Global Biogeochemical Cycles

RESEARCH ARTICLE
10.1029/2025GB008803

Upper Ocean Cycling of Iron South of the Polar Front: Biological Patterns and Processes

Luis M. Laglera[1,2], Juan Santos-Echeandía[3], Viena Puigcorbé[4,5], Christine Klass[6], and Dieter Wolf-Gladrow[6]

[1]Departamento de Química, FI-TRACE, Universidad de las Islas Baleares, Palma, Spain, [2]Laboratori Interdisciplinar sobre Canvi Climátic, Universidad de las Islas Baleares, Palma, Spain, [3]Centro Oceanográfico de Vigo, Instituto Español de Oceanografía (IEO-CSIC), Vigo, Spain, [4]Department of Marine Biology and Oceanography, Institut de Ciències del Mar (ICM-CSIC), Barcelona, Spain, [5]Centre for Marine Ecosystems Research, School of Science, Edith Cowan University, Joondalup, WA, Australia, [6]Alfred-Wegener-Institut Helmholtz Zentrum für Polar- und Meeresforschung, Bremerhaven, Germany

Abstract Samples from the upper 300 m along the 52°S band, south of the Antarctic Polar Front in the Atlantic sector of the Southern Ocean, including a 3-week monitoring of a persistent bloom, were analyzed to advance our understanding of iron cycling and supply to recurrent phytoplankton blooms. We measured dissolved Fe (dFe, <0.2 μm) and labile particulate iron using a mild acid leach ($pLFe^{48h}$) targeting primarily detrital and fecal material. Particulate iron was partitioned into size classes to distinguish small, "slow" sinking particles (<53 μm) from large, "fast" sinking particles (>53 μm), while intermediate fractions were analyzed to investigate aggregation and export processes. Across all stations, dFe exhibited a consistent vertical structure, including a previously undescribed ubiquitous minimum below mixed and euphotic layers. The absence of $pLFe^{48h}$ in the 0.2–3 μm fraction indicates reduced aggregation and is consistent with minimal authigenic Fe formation. Instead, $pLFe^{48h}$ was concentrated in "slow" sinking particles, indicating surface entrainment. Biomass was negatively correlated with dFe but positively correlated with $pLFe^{48h}$, linking bloom development to particulate iron availability rather than dFe. Overall, rapid surface recycling of "slow" sinking $pLFe^{48h}$ appeared to meet most of the daily iron demand during a prolonged diatom bloom. Near South Georgia Island, wind-driven mobilization of iron-rich material from the island snowpack and deposition into leeward waters likely supplied an additional iron source. By applying new protocols to characterize labile particulate iron, we reveal the elusive magnitude of the recycling dynamics of particulate iron in fecal and detrital materials sustaining Southern Ocean blooms.

Plain Language Summary Owing to its scarcity, iron is crucial in regulating life distribution across large regions of the ocean surface. Yet in the Atlantic sector of the Southern Ocean, the mechanisms supplying iron to support the region's frequent phytoplankton blooms remain insufficiently understood. To investigate these processes, we applied a mild acidification method to filtered and unfiltered seawater, allowing us to determine iron in particles such as fecal material and cellular debris aggregates, apart from cellular and mineral forms. This approach revealed an unexpected, widespread minimum of dissolved iron just below the sunlit surface layer (60–100 m), alongside a predominance of detrital and freshly formed particulate iron within "slow-sinking" particles. This combination is critical for recycling particulate iron in surface waters before iron sinks too deep for photosynthetic organisms' reutilization. Additionally, strong winds over South Georgia Island likely resuspended iron-rich particles trapped in snow on the island's crest, adding more iron to nearby waters. This research highlights the importance of recycled biological particles in sustaining ocean productivity and emphasizes the need for novel analytical protocols to study how iron moves through diverse particle types in the ocean.

Key Points:

- Dissolved iron showed a consistent subsurface minimum just below the mixed and euphotic layers across contrasting biochemical regimes
- Slow-sinking leachable particulate iron supplied bioavailable iron to local blooms, with additional input leeward of South Georgia from wind
- Rapid recycling of fecal and cellular debris, but not authigenic Fe, supplies bioavailable Fe for blooms

Supporting Information:

Supporting Information may be found in the online version of this article.

Correspondence to:

L. M. Laglera,
luis.laglera@uib.es

Citation:

Laglera, L. M., Santos-Echeandía, J., Puigcorbé, V., Klass, C., & Wolf-Gladrow, D. (2026). Upper ocean cycling of iron South of the Polar Front: Biological patterns and processes. *Global Biogeochemical Cycles*, *40*, e2025GB008803. https://doi.org/10.1029/2025GB008803

Received 30 JUL 2025
Accepted 6 APR 2026

Author Contributions:

Conceptualization: Luis M. Laglera, Dieter Wolf-Gladrow
Data curation: Luis M. Laglera
Formal analysis: Luis M. Laglera, Juan Santos-Echeandía
Funding acquisition: Luis M. Laglera
Investigation: Luis M. Laglera, Christine Klass
Writing – original draft: Luis M. Laglera
Writing – review & editing: Juan Santos-Echeandía, Viena Puigcorbé, Christine Klass, Dieter Wolf-Gladrow

1. Introduction

Understanding how trace elements cycle through the ocean is central to unraveling the links between marine productivity, carbon sequestration, and climate regulation. Over the past decades, advances in clean sampling and trace analysis, particularly through the GEOTRACES program (Anderson, 2020), have greatly expanded our understanding of trace element distribution across diverse ocean basins (Schlitzer et al., 2018). This progress has revealed that processes such as size fractionation between dissolved and particulate forms, organic complexation,

particle adsorption, and precipitation shape the chemical speciation, reactivity, and bioavailability of trace elements (Gledhill & Buck, 2012; Seo et al., 2022; von der Heyden & Roychoudhury, 2015).

Building on this understanding, recent efforts have sought to explore the partition of trace elements between dissolved (i.e., species passing through a 0.2 μm filter) and particulate (>0.2 μm) phases across different size classes. Fractionation studies have traditionally focused on <0.2 μm size classes under the assumption that truly dissolved forms (measured after ultrafiltration) represent the bioavailable pool (Fitzsimmons et al., 2015). However, growing interest in the particulate fraction, which is typically analyzed by digesting filters with strong acids and microwave-assisted extraction (Chen et al., 2004; Wen et al., 1996), has highlighted its importance in scavenging and as a source of dissolved trace elements after remineralization (Twining, 2024). Some studies refine this approach further by applying milder leaching protocols, using less acidic conditions and/or reducing reagents, to differentiate labile from refractory (chemically inert) particulate forms (Berger et al., 2008; Schlosser et al., 2018). Nonetheless, size fractionation using pore sizes cutoffs of ≥0.2 μm or ≥0.45 μm, a common approach in marine ecology to categorize plankton (Flynn et al., 2025) and in the study of particulate organic carbon export using radioisotopes (Buesseler et al., 2020), remains rare in open ocean studies (Frew et al., 2006; Lemaitre et al., 2020; Planquette et al., 2013), which often operationally define particulate iron as >0.45 μm (Cutter et al., 2017). Consequently, the nature of trace element-bearing particles is often inferred indirectly using (a) elemental ratios, such as Fe/Al, to estimate and subtract the terrigenous component (Frew et al., 2006; Lannuzel et al., 2014), (b) stoichiometric measurements of trace elements relative to phosphorus or carbon in phytoplankton or bulk particulate organic carbon (POC) (de Jong et al., 2012), or (c) dust collection and solubility experiments (Ito & Shi, 2016). The continuous exchange of trace elements between dissolved and particulate phases, via processes such as uptake, remineralization, and transformation into bioavailable forms, remains poorly quantified.

Most studies of oceanic metal concentrations and distributions rely on depth profiles collected along planned transects (also referred to as sections). These data sets form the foundation of our current understanding of trace element biogeochemistry in the ocean (Schlitzer et al., 2018). However, trace element distributions are shaped by highly dynamic physical, chemical, and biological factors that can vary on timescales of hours to days (Boyd et al., 2005), much faster than the time required to complete a transect. Monitoring temporal changes within a single water mass is generally limited to incubation or large-scale perturbation experiments, such as ocean iron fertilizations (Laglera et al., 2017; Nishioka et al., 2005). These studies have shown that changes in biomass, community composition, and grazing pressure can alter both trace element concentrations and chemical speciation (Croot & Laan, 2002; Kondo et al., 2008; Laglera et al., 2020).

A critical but often overlooked aspect of interpreting trace element data is the integration of process timescales. As in consecutive chemical reactions, the slowest biogeochemical process can control ocean fluxes and inventories. For instance, the contribution of slow dust dissolution to dissolved iron (dFe) concentration, occurring over many weeks (Mendez et al., 2010), competes with faster physical and biological processes, such as biological uptake (Shaked & Lis, 2012). This mismatch can lead to misinterpretation of diffusive and trophic fluxes; for example, vertical dFe gradients, often used to estimate long-term upward diffusion from depth (Croot et al., 2007; de Jong et al., 2012), may partly reflect faster in situ dissolution of sinking particles. Furthermore, the extent and kinetics of trace element recycling within the mixed layer (ML) remain incompletely quantified, particularly regarding particulate–dissolved transfers as a function of the particle biochemical nature (Boyd et al., 2010). Particle residence times in the ML are influenced by geophysical factors (e.g., sinking rates), chemical transformations (e.g., formation of iron oxyhydroxides) (Johnson et al., 1997; Misumi et al., 2021) and biological processes (e.g., colloid phagotrophy by flagellates) (Barbeau et al., 1996; Maranger et al., 1998). POC export also modulates the standing stocks and cycling of associated trace elements in the ML. However, current analytical approaches rarely distinguish particulate trace element concentrations by their biochemical nature, limiting our understanding of their distinct roles in upper ocean cycling and how POC export contributes to variability in ML trace element inventories (Boyd et al., 2010).

Clarifying these processes is especially important in the Southern Ocean, a region critical for global climate regulation and carbon cycling (Sabine et al., 2004). The complex interplay of physical mixing, eddies, and water mass interactions complicates the identification of trace element sources, sinks, and cycling. Despite high macronutrient concentrations year-round, primary productivity, and therefore CO_2 fixation, is frequently limited by iron availability (de Baar et al., 1995; Morrison et al., 2015; Smetacek et al., 2012). Recently, complexity was

added as other bioactive elements such as Co, Cu, and Mn have also been proposed as potential co-limiters (Browning & Moore, 2023; Browning et al., 2021; de Baar et al., 1995). Yet, large portions of the Southern Ocean remain under-sampled for trace elements due to its remoteness.

The Eddy-Pump campaign was conducted in the Atlantic sector of the Southern Ocean, along the Antarctic Circumpolar Current (ACC), south of the Antarctic Polar Front within a latitudinal band around 50° to 52°S, and extending from 10°E to 39°W (Hoppe et al., 2017; Strass, Wolf-Gladrow, et al., 2017; Strass, Leach, et al., 2017). This region is characterized by dynamic frontal systems, variable silicate and biomass distributions, and poorly constrained iron supply mechanisms (Hoppe et al., 2017; Strass, Wolf-Gladrow, et al., 2017; Strass, Leach, et al., 2017). Here, we present vertical profiles of dissolved and particulate Fe in the upper 300 m, using a high depth resolution designed to resolve fine-scale variability in upper-ocean iron distribution. Particulate iron concentrations were measured in both bulk unfiltered seawater and in >0.2 μm fractions using a novel leaching protocol (48 hr at pH 2.0). This approach allowed us to elucidate authigenic iron formation and distinguish between "slow" and "fast" sinking particle pools. These observations allow us to investigate how biologically mediated processes shape the cycling of Fe in this climatically significant region of the Southern Ocean, with particular emphasis on the role of different particulate Fe forms in sustaining bloom development.

2. Materials and Methods

2.1. Study Region

Sampling was conducted during the Eddy-Pump campaign onboard the RV Polarstern (ANT-XXVIII/3) in the Atlantic sector of the Southern Ocean between January and March 2012 (Strass, Wolf-Gladrow, et al., 2017; Wolf-Gladrow, 2013). The cruise track followed a westward path along the latitude band of approximately 52°S, within the eastward flowing Antarctic Circumpolar Current (ACC) (Figure 1a). Onboard incubation experiments conducted with and without iron additions demonstrated that primary productivity was limited by iron availability (Trimborn et al., 2017). Except where explicitly noted, the physical, chemical, and biological information presented in this section is drawn from previously published studies of this cruise and is cited accordingly.

Several sampling locations at the specified latitudes were selected between 10°E and 39°W (Figure 1a), based on the distinctive physical and biological features encountered:

i) Location A comprised two stations located at 10°E, 52° and 53°S, respectively. Both stations were south of the PF in an area of strong eastward currents (Strass, Leach, et al., 2017). A detailed description of the physical and biochemical conditions may be found elsewhere (Cheah et al., 2017; Puigcorbé et al., 2017; Strass, Leach, et al., 2017). Briefly, the ML, extending down to 90 m at 52°S and 55 m at 53°S, was characterized by moderately high Chl *a* concentrations (0.61 ± 0.15 mg m^{-3}, Figure 1b), and moderate photosynthetic efficiency (F_V/F_M, an indicator of iron deficiency) values (0.36 ± 0.04). The phytoplankton community was dominated by diatoms, and the zooplankton community was mostly comprised of salps, with a minor contribution from euphausiids (Pakhomov & Hunt, 2017). At this location, the Upper Circumpolar Deep Water (UCDW), characterized by reduced oxygen concentrations, intruded into the epipelagic layer, enriching the ML with nutrients, including silicate (Puigcorbé et al., 2017).

ii) Location B. At 8°W 52°S, we found a 71 m deep ML characterized by very low Chl *a* concentrations (<0.11 mg m^{-3}) despite high concentrations of all nutrients including silicate (Hoppe et al., 2017). The zooplankton community was defined by an exceptionally high abundance of the salp *Salpa thompsoni* (catch of 2.15 WW g salp m^{-3}) (Hoppe et al., 2017; Pakhomov & Hunt, 2017; Wolf-Gladrow, 2013).

iii) Location C. Sailing westward from location B, we encountered a strong gradient of surface Chl *a* concentrations on January 29th, entering an area with a long-lasting large-scale phytoplankton bloom (12°W 51°S). Stations inside and outside of the bloom core were sampled over 3 weeks (Hoppe et al., 2017; Roca-Martí et al., 2017; Strass, Leach, et al., 2017). The bloom was visible in satellite Chl *a* images from mid-December onward and peaked approximately 2 weeks before our arrival (Hoppe et al., 2017). Despite the distance from islands and aerial sources of iron, Chl *a* concentrations reached up to 2.7 mg m^{-3} upon our arrival (Figure 1c). Repeated occupations of the central station at Location C over the 3-week sampling period revealed a persistent upper-ocean structure, with a well-defined Winter Water (WW) temperature minimum near 150 m and deeper underlying UCDW (Strass, Leach, et al., 2017). Although temporal variability was observed in ML depth and in the vertical structure below the WW during the latter part of the occupation, these changes were largely density-compensated and occurred within a coherent water-mass framework (Strass, Leach,

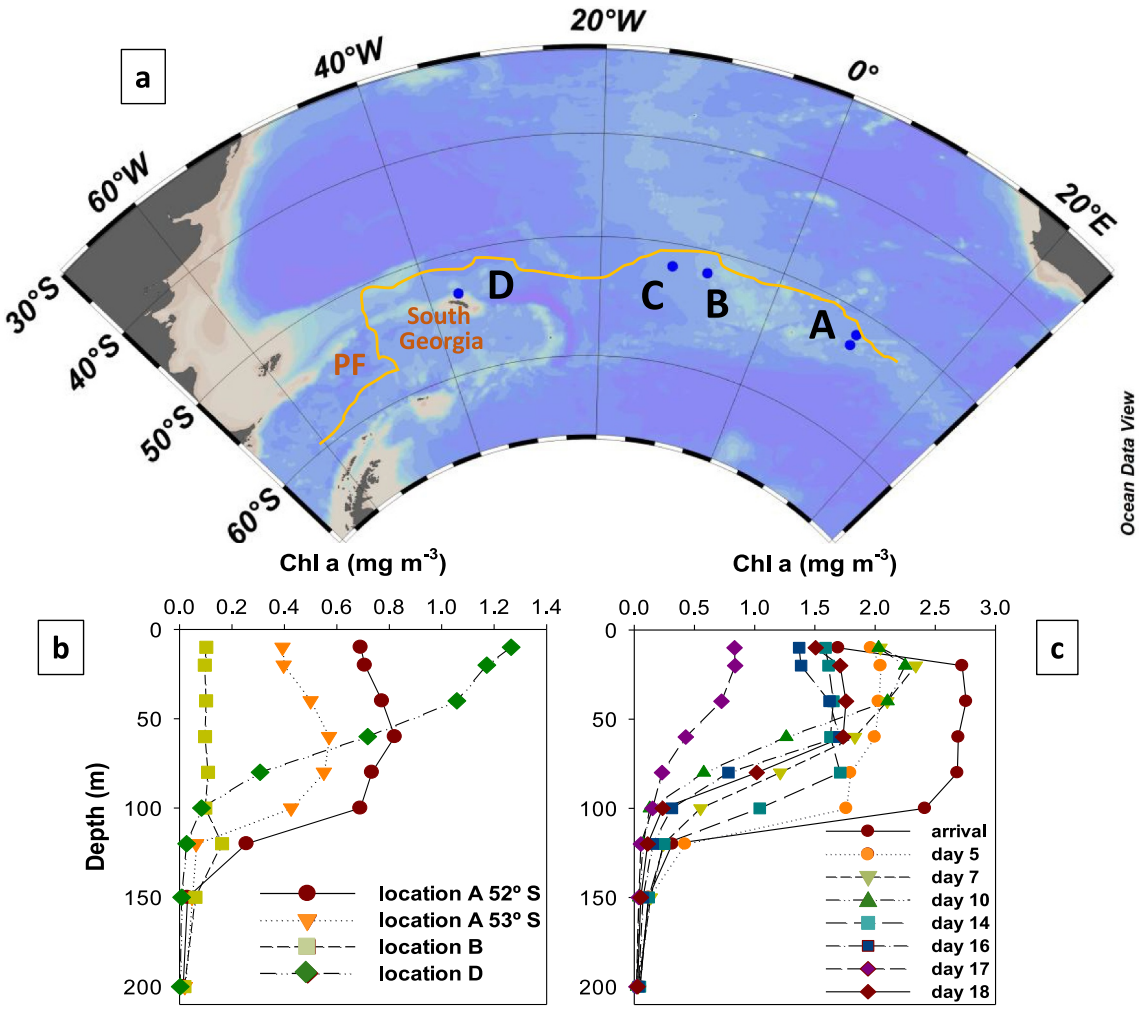

Figure 1. (a) study area and location of sampled stations (Ocean Data View). In yellow, the Polar Front path. (b) Chl *a* concentrations measured at locations A, B and D. (c) Time series of Chl *a* concentrations at location C.

et al., 2017). Weak mesoscale variability in the region manifested as a poorly developed meander, and currents remained relatively steady throughout the study period. Together, these observations indicate that the time series predominantly sampled a single bloom system and a broadly coherent water parcel (Strass, Leach, et al., 2017). Detailed information on the evolution of the ML and euphotic zone depths, nutrient utilization, POC and primary productivity can be found in the previous publications from this cruise (Hoppe et al., 2017; Roca-Martí et al., 2017; Strass, Leach, et al., 2017) and is discussed in Sections 4.3 and 4.6. Low-oxygenated UCDW was not detected above 500 m and therefore had a minimum impact on our study (Roca-Martí et al., 2017; Strass, Leach, et al., 2017). For the 3 weeks following our initial sampling, Chl *a* concentrations remained high (1.5–2 mg m^{-3}) but never returned to the initial value (Figure 1). This was likely due to a combination of the bloom decline, biomass spatial variability (declining from the northwest towards the southeast in the study area), dilution by wind-driven deep mixing under bad weather conditions, and difficulties in locating the area with maximum Chl *a* within the bloom (Wolf-Gladrow, 2013). Macronutrient concentrations were approximately constant (Figure S1 in Supporting Information S1) despite the shallow euphotic layer (30 ± 8 m) (Hoppe et al., 2017) and the variability of the ML depth (36–89 m, Figure 2) (Strass, Leach, et al., 2017) and were characterized by very low silicate concentrations and moderate nitrate and phosphate deficits, possibly due to a low availability of iron (Hoppe et al., 2017). The primary producer community was dominated by diatoms (Hoppe et al., 2017; Wolf-Gladrow, 2013).

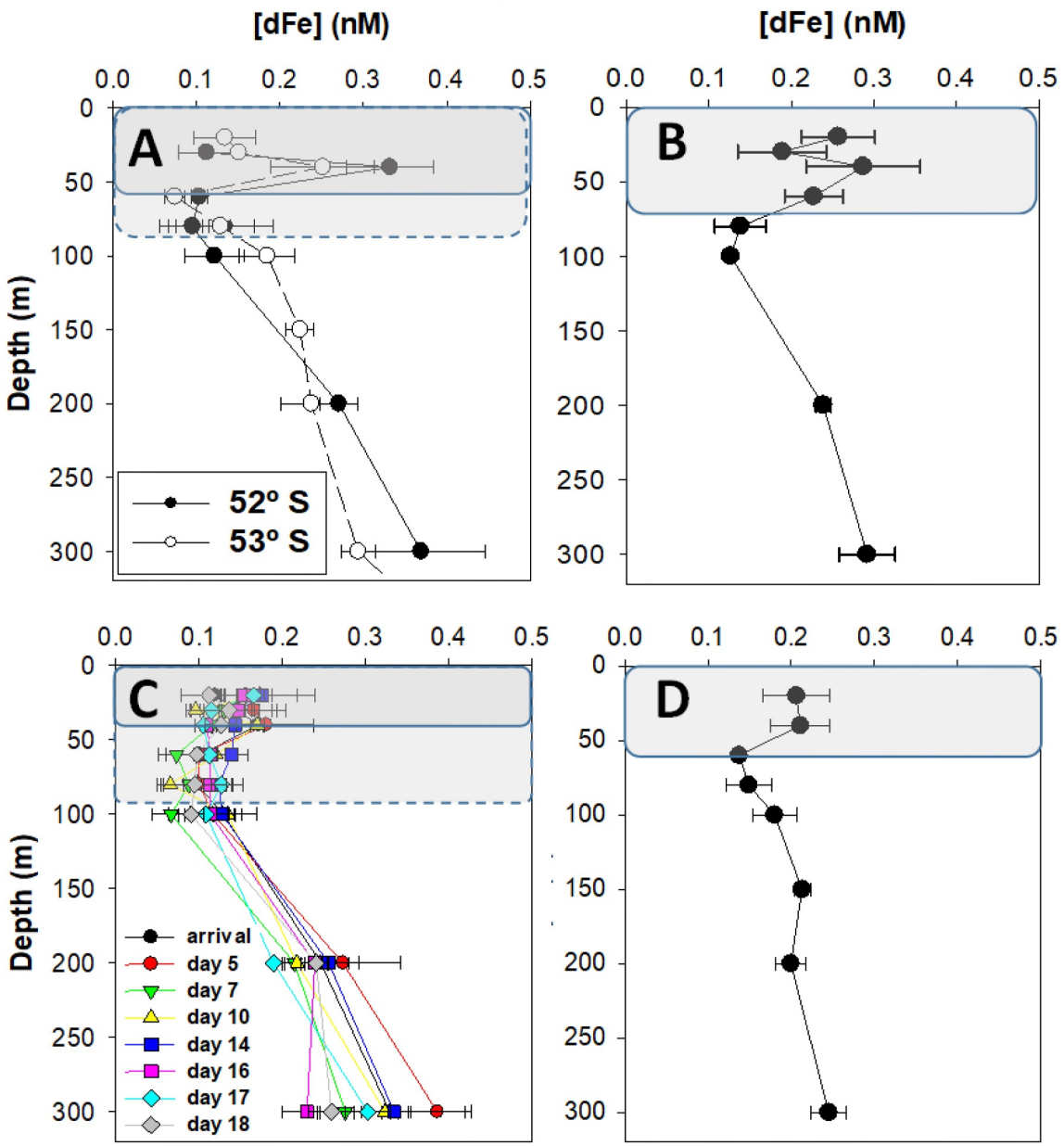

Figure 2. A–D: Dissolved iron concentrations (<0.2 μm) in the upper 300 m at the four locations (A–D) sampled during the ANT-XXVIII/3 cruise. The mixed layer is shaded in gray. A: solid contour, 52°S; dashed contour, 53°S; C: solid contour, minimum value of 36 m on day 7, dashed contour, maximum value of 89 m on arrival.

iv) Location D. One station in the continental shelf slope of South Georgia at 53°30′S and 36°24′W (depth of 1,270 m), approximately 80 km north of Grytviken, is located leeward of the prevailing westerly winds (Figure 1). Data collected at this station have not been included in any previous publication.

2.2. Clean Sampling

Samples were collected following standard clean procedures from the upper 300 m of the water column by means of eight Teflon coated GOFLO bottles attached to a Kevlar line (Cutter et al., 2017). Once onboard, the GOFLO bottles were immediately transferred to a clean plastic bubble, pressurized with 0.2 μm filtered high purity N_2 and subsamples collected in 125 mL acid-cleaned low-density polyethylene (LDPE, Nalgene) bottles. At all stations, we collected unfiltered and filtered by 0.2 μm fractions, the last by means of passing the seawater through filtration sterile capsules (Sartobran 300) using Masterflex C-Flex tubes (Cole-Palmer). From day 5 of sampling

at location C onwards, we further collected a third fraction by replacing the 0.2 μm capsules with a single filter holder fitted with different pore size filters. On days 5 and 7 and on days 10 and 14 (all at location C), we used 0.4 and 3 μm pore size cellulose acetate filters (Millipore). On days 16–18 at location C and at location D we used 53 μm nylon screens (Nitex).

2.3. On Board Analysis of Iron

For on-board analysis of Fe, we used adsorptive cathodic stripping voltammetry (AdCSV) on samples acidified overnight, using a 663 VA stand (Metrohm AG), controlled by a μAutolab voltammeter (Eco Chemie B.V.). A detailed account of the method can be found in Laglera et al. (2013). Briefly, sampling bottles (125 mL) with filtered or unfiltered samples were immediately acidified by addition of 12 μL HCl (30% Ultrapur, Merck) per 10 mL seawater for a pH of 2.0 (NBS scale) and spiked with 2,3-dihydroxynaphthalene (DHN, Merck) to a final concentration of 30 μM. Subsamples filtered by 0.2 μm were analyzed for dFe the following day (Laglera et al., 2013). Subsamples filtered through other pore sizes (see Section 2.4) or left unfiltered were analyzed after 2 days of acidification (rationale in Section 4.4). Accurate data interpretation requires understanding that cathodic voltammetric techniques respond only to analyte species capable of migrating to, adsorbing onto the electrode surface, and being reduced following a potential switch. Therefore, the method is not reactive to any sort of iron that remains within particles, and the signal is the result of all the dissolved and adsorbed species that are dissociated after acidification and later forced to react with excess concentration of DHN immediately before analysis. According to the sample strategy, we define the following fractions:

- dFe: as the total dissolved concentration of iron (<0.2 μm).
- $tLFe^{48h}$: "total" leachable Fe of unfiltered or filtered using pore sizes >0.2 μm samples (detailed in Section 2.4) after 48 hr of acidification with HCl to pH 2.0.
- $pLFe^{48h}$: particulate leachable Fe after 48 hr of acidification to pH 2.0 calculated from the difference between $tLFe^{48h}$ and dFe ($tLFe^{48h}$–dFe).

The tLFe fraction increases extending the acidification period (>48 hr) while this was not the case for dFe.

Immediately before analysis, a 10 mL subsample was spiked with 500 μL of a combined BrO_3^-/POPSO (piperazine-N,N′-bis-(2-hydroxypropanesulfonic) acid) catalytic/buffer solution (0.4 and 0.1 M, respectively) and the volume of a NH_4OH solution (15%, UltraTrace, Sigma) required to raise the pH to ∼8.7 (Laglera et al., 2013). Each sample was analyzed in at least duplicate, and each analysis was calibrated using two internal standard additions: 0.2 nM Fe for dissolved samples, and 0.3–2 nM Fe for the remaining samples, with the latter concentrations selected based on the initial electrochemical signal. All uncertainties from the analysis of duplicates or triplicates are expressed as one standard deviation (±1σ).

AdCSV settings were 90 s deposition at 0 V, quiescence period of 7 s and a potential scan from −0.1 to −1.15 V at 50 mV s^{-1} (step increment of 5 mV and 10 steps s^{-1}). Reagent blanks gave values in the range 0.06–0.10 nM after analysis of ultrapure water at the regular and triple reagent concentrations.

GEOTRACES consensus samples SAFe surface (S) and deep (D2) were analyzed repeatedly during the cruise, yielding concentrations of 0.12 ± 0.02 nM (n = 4) for the S sample (consensus value 0.096 ± 0.008 nM) and 1.04 ± 0.12 nM (n = 7) for the D2 sample (consensus value 0.959 ± 0.059 nM) (Johnson et al., 2007).

2.4. Iron Size Partitioning

Starting on day 5 of sampling at location C, we collected an additional size fraction from each sample to infer the nature of the particles that released iron following our leaching protocol (sampling scheme in Figure S2 in Supporting Information S1). Due to operational constraints, it was not feasible to include additional fractions from the same cast. Therefore, at location C, on days 5 and 7, we collected a <0.4 μm fraction to monitor the possible aggregation of iron in colloids >0.2 μm that could eventually lead to scavenging. On days 10 and 14, we collected a <3 μm fraction to further study aggregation and the possible contribution of small cells to $pLFe^{48h}$. For the remainder of the cruise, we collected a <53 μm fraction, which is the cut-off size used for ^{234}Th-based carbon export studies (Puigcorbé et al., 2017). To clarify their different potential roles in vertical processes, we decided to label the 0.2–53 μm and >53 μm fractions as "slow" and "fast" sinking $pLFe^{48h}$, respectively.

Table 1
Integrated NPP in the Upper 100 m and Standing Stocks in the Upper 100 m of Chl a, POC, dFe, and pLFe^{48h} at Selected Stations During the Eddy Pump Cruise

Location	Chl a mg m^{-2}	POC mol m^{-2}	NPP mol m^{-2} d^{-1}	dFe µmol m^{-2}	pLFe^{48h} µmol m^{-2}
A—52°S	75.2	0.80	0.073	14.1	28.8
A—53°S	49	0.75	0.074	14.5	56.5
B	10.1	0.56	0.013	21.2	20.1
C—arrival	256	2.16	0.216	12.3	61.1
C—day 5	198	1.56[a]	0.235	13.5	77.3
C—day 7	176	1.57[b]	n.a.	10.8	39.1
C—day 10	146	1.55	0.204	12.9	44.8
C—day 14	160	1.50	0.139	14.6	17.6
C—day 16	128	1.40	0.088	12.6	52.6
C—day 17	55.1	0.86	0.066	12.8	28.2
C—day 18	143	1.33	0.167	10.8	39.5
D	74.4	1.06	n.a.	17.9	186

[a]POC not analyzed on day 5. Samples taken on day 6. [b]POC not analyzed on day 7. Samples taken on day 8.

2.5. Iron Leaching From Unfiltered Samples Collected at Location D

Due to the distinctive pLFe^{48h} profile found at location D, suggestive of aeolian input, we stored samples at pH 2.0 and room temperature, reanalyzing them 12 days later onboard and again after 118 days in the lab. This aimed to assess whether leaching kinetics at pH 2.0 could inform on the nature of iron-bearing particles (Laglera et al., 2017). The same analytical protocol and equipment described in Section 2.3 were used.

3. Results

3.1. Dissolved Iron Concentrations and dFe Stratification in the ML at Locations A, B, and C

Dissolved iron concentrations in the upper 300 m were consistently within a range of 0.09–0.4 nM (Figures 2a–2c). At location C, dFe profiles in the upper 300 m were remarkably consistent over a 3-week period (Figure 2c).

Focusing on our high resolution depth profiles, a consistent stratification pattern emerged in the upper 300 m. In the upper 50 m and below 150 m, dFe concentrations were higher, ranging from 0.2 to 0.4 nM. Between 60 and 100 m, concentrations were lower, around 0.1 nM or below (Figure 2). This pattern was stable during our sampling at location C where dFe average concentrations in the upper 40 m and 60–100 m layers were 0.142 ± 0.025 nM and 0.106 ± 0.020 nM, respectively. The significance of the difference between these two groups was confirmed by a *t*-test: $t = 5.45$; $p < 0.001$; 46 degrees of freedom. From 100 to 300 m (500 m in the case of location A/53°S, [dFe] = 0.60 nM), dFe concentrations showed a linear increase with depth (Figure 2).

For comparison between different locations, we will use standing stocks of chemical species in the upper 100 m (the total amount of the chemical species integrated within the upper 100 m at a given time) that for dFe values at station A were 14.1 and 14.5 µmol m^{-2} at 52°S and 53°S, respectively. The dFe standing stocks were higher at location B (21.2 µmol m^{-2}), and lower at location C, ranging from 10.8 to 15.0 µmol m^{-2}. The dFe standing stock at location D was 17.9 µmol m^{-2} (Table 1).

3.2. Leachable Particulate Iron Variability at Locations A, B, and C

Vertical profiles of the tLFe^{48h} fraction in the upper 100 m exhibited high inter-location variability (Figure 3). In this layer, where dFe concentrations were found ranging in a four-fold range between ~0.1 and 0.4 nM, pLFe^{48h} concentrations varied nearly two orders of magnitude, from near depletion at 0.03 nM (location B, 80 m deep) to 2.30 nM (location C, day 0, 30 m deep). The relative contribution of pLFe^{48h} varied widely, accounting for between 40% and 90% of the tLFe^{48h} pool.

At location A, pLFe^{48h} was virtually absent in the upper 60 m at the 52°S station but increased substantially below 50 m, whereas at the 53°S station, pLFe^{48h} was consistently higher throughout the entire depth range (Figure 3). Correspondingly, the standing stocks of pLFe^{48h} at these two stations (28.8 and 56.5 µmol m^{-2}, respectively), were approximately two- and four-fold higher than the corresponding dFe standing stocks. At location B, pLFe^{48h} was nearly absent throughout the upper 100 m (range 0.03–0.11 nM), except for a single high value of 0.6 nM at 20 m. This resulted in a pLFe^{48h} standing stock of 20.1 µmol m^{-2}, comparable to the dFe standing stock (Figure 3 and Table 1). At location C, pLFe^{48h} at 20 and 30 m showed significant variability. On days 0, 5, 17, and 18, pLFe^{48h} high concentrations were up to 0.25 nM, while on days 7, 10, 14 and 16 this signal was very low (shaded area in Figure 3). Below 30 m, vertical pLFe^{48h} profiles showed no distinctive features across all sampling days, with concentrations remaining relatively uniform with depth. Overall, pLFe^{48h} standing stocks in the upper 100 m varied four-fold, ranging from 20.1 to 77.3 µmol m^{-2}, and exceeded dFe standing stocks by two- to five-fold (Table 1).

Below 100 m, pLFe^{48h} concentrations at locations A–C showed variability although no clear vertical trend with depth was apparent (Figure 3).

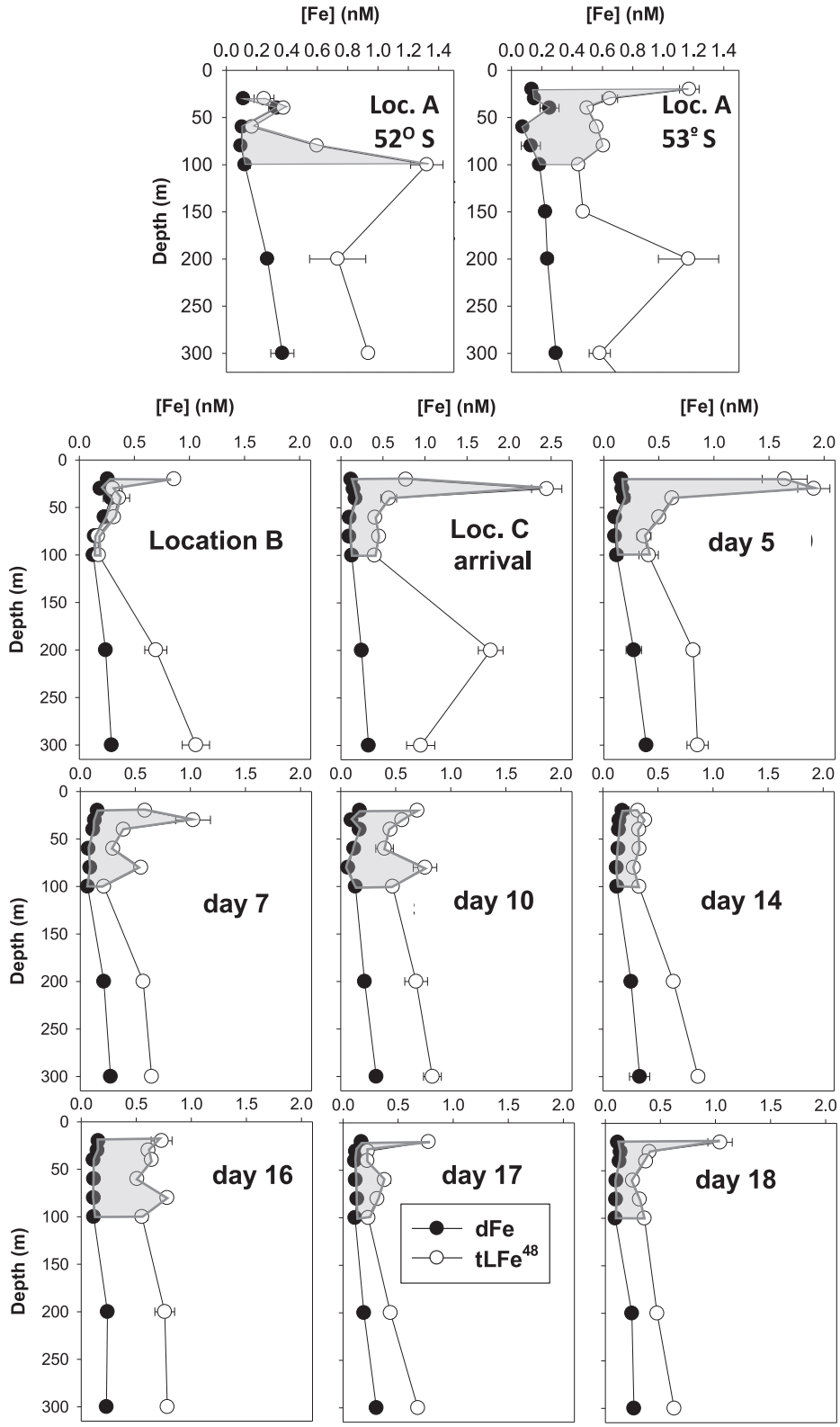

Figure 3. Vertical profiles of dissolved iron (dFe, •) and iron leached in unfiltered samples after 48hr acidification at pH 2.0 ($tLFe^{48h}$, ○) at locations A, B and C. The gray shaded area highlights the concentration of $pLFe^{48h}$ in the upper 100 m, the depth of integration used to calculate standing stocks.

3.3. Iron Size Partitioning at Location C

From day 5 of sampling at location C onwards, we collected a third fraction using a second filter (0.4 μm, 3 μm or 53 μm) to study iron aggregation and differentiate "fast" and "slow" sinking particles labile to our leaching protocol.

The fractionation results at location C are shown in Figure 4 with the contribution of each fraction to $tLFe^{48h}$ shown in Figure S3 in Supporting Information S1. On days 5 and 7, $pLFe^{48h}$ in the size fraction 0.2–0.4 μm was negligible, except for minor concentrations at 80–100 m, where it contributed 5%–30% of $tLFe^{48h}$. On days 10 and 14, $pLFe^{48h}$ in the 0.2–3 μm range was similarly negligible, except for a minor $pLFe^{48h}$ contribution to $tLFe^{48h}$ of 5%–20% at 80–100 m. The use of 53 μm screens revealed a more complex pattern. On day 16, the shift of the intermediate fraction (red dots in Figure 4) indicates the presence of significant fractions of both "slow" and "fast" sinking $pLFe^{48h}$ across all depths, contributing 45 ± 10% and 33 ± 14% to $tLFe^{48h}$, respectively. During the last 2 days of sampling at location C, the "fast sinking" $pLFe^{48h}$ was reduced to 9 ± 11% and 19 ± 19%, respectively (Figure 4 and Figure S4 in Supporting Information S1).

3.4. Location D. Iron Partitioning, Particle Leaching Kinetics, and Oceanographic Variables

Departing from South Georgia, we observed high Chl *a* concentrations and F_V/F_M values from the continuous surface seawater supply of the ship in the ranges 1.0–1.4 mg m^{-3} and 0.4–0.5, respectively (Figure S4 in Supporting Information S1) and decided to carry out a single trace-metal clean cast (location D). The ML was 59 m deep and the vertical Chl *a* and transmittance profiles indicated a shallower distribution of biomass compared to other locations (Figure 1b).

Location D lies at the northeast edge of South Georgia's continental shelf (Figure 1). The wind speed and direction recorded by the two local meteorological stations during the 4-day period preceding our sampling are shown in Figure S3 in Supporting Information S1. The Bird Island meteorological station recorded winds with an average speed of 4.8 ± 2.2 m s^{-1}, predominantly from the SSW direction (213° ± 49°). In contrast, the Grytviken station recorded winds with an average speed of 5.2 ± 2.0 m s^{-1}, primarily from the W direction (289° ± 27°). These discrepancies are likely due to the sheltering effect provided by the island ridge to King Edward Cove. Winds recorded by the RV Polarstern meteorological station (taken partially in transit) from the day before sampling upon arrival in King Edward Cove until departing from location D, were substantially stronger, averaging 9.3 ± 2.5 m s^{-1} with a WSW direction of 258° ± 18.

The dFe vertical profile followed the features found at the other locations with slightly higher concentrations in the upper part of the ML, a poorly defined minimum at the lower part of the ML and an increase down to 300 m (Figure 2). However, $pLFe^{48h}$ concentrations were substantially higher with a distinctive profile defined by an exponential decrease with depth (Figure 5). Partitioning with 53 μm screens showed that as it was the case for the last 2 days at location C, $pLFe^{48h}$ concentrations in the upper 150 m leached entirely from "slow" sinking particles , whereas in the 200 and 300 m deep samples, approximately half of $pLFe^{48h}$ was in "fast" sinking particles (Figure S4 in Supporting Information S1).

Due to the uniqueness of these profiles, we reanalyzed the samples twice over an extended period to try to infer from variations in leaching kinetics if iron leaching particles were of different natures depending on the sampling depth and their sinking rate (i.e., "slow" vs. "fast" sinking). Reanalysis after 12 and 118 days showed that $pLFe^{48h}$ concentrations in the fractions filtered by 53 μm and unfiltered increased approximately two- and four-fold, respectively, at all depths (Figure 5). The extension of the acidification time did not change the $pLFe^{48h}$ size partitioning, with a significant presence of "fast" sinking $pLFe^{48h}$ only below 150 m. Figure 5 (bottom) shows that the leaching kinetics of "slow" and "fast" sinking $pLFe^{48h}$, normalized to concentration on day 118, were similar regardless of the sampling depth (see discussion in Section 4.6).

4. Discussion

4.1. Comparison With Prior Studies South of the Antarctic Polar Front

The remote nature of our area of study has led to limited coverage by GEOTRACES or other national or international scientific programs, allowing direct comparison with other cruises only at location A, situated 10° east of the GIPY05 transect (Klunder et al., 2011; Sieber et al., 2021). At location D, two cruises reported dFe

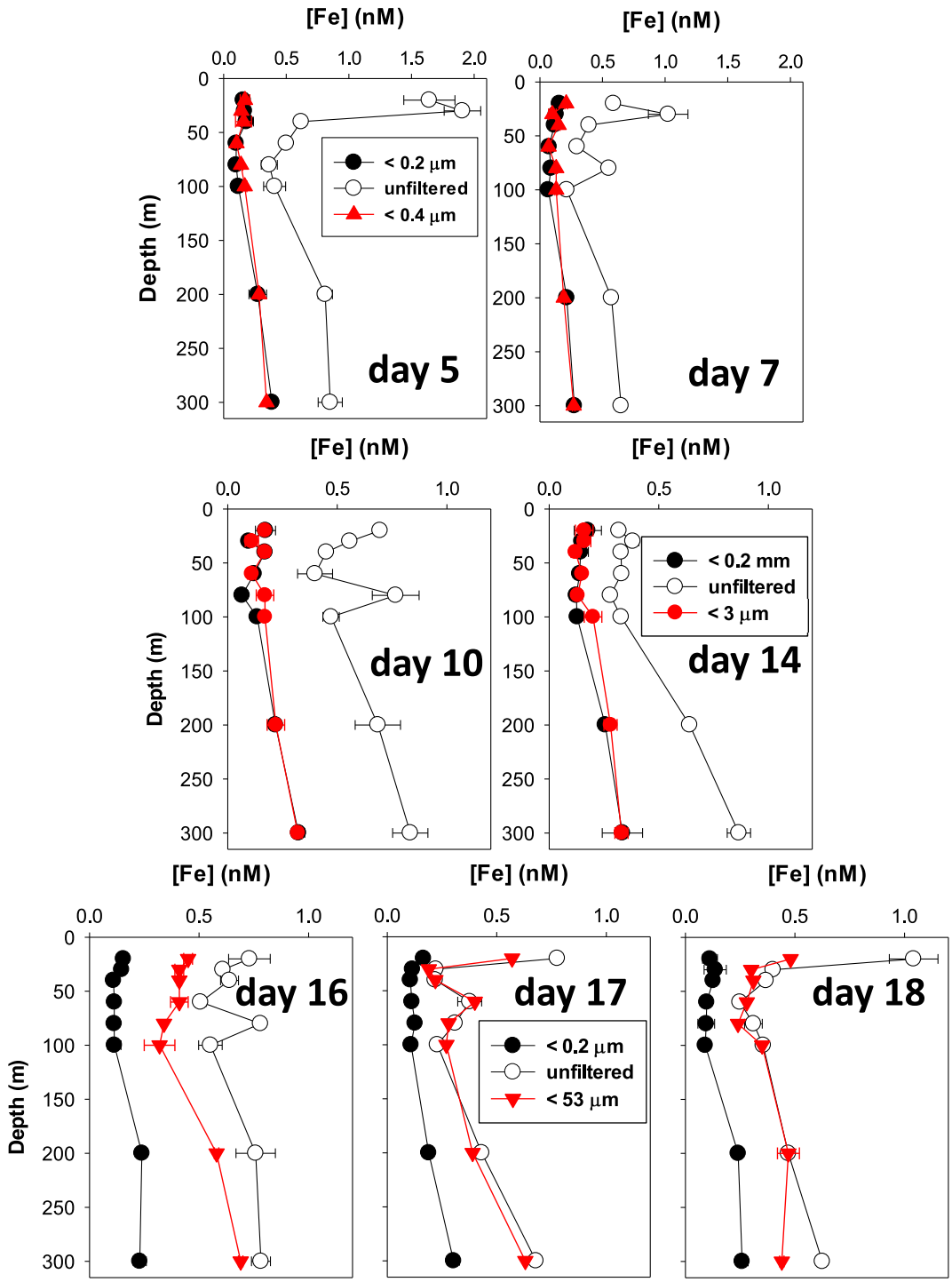

Figure 4. Location C: vertical profiles of iron concentrations leached after 48 hr at pH 2.0 ($pLFe^{48h}$) in three operationally defined fractions. On days 5 and 7 (top), fractions include <0.2 µm, <0.4 µm, and unfiltered; on days 10 and 14 (middle), <0.2 µm, <3 µm, and unfiltered; and on days 16–18 (bottom), <0.2 µm, <53 µm, and unfiltered. The progressive shift of the red symbols from alignment with dissolved Fe concentrations to alignment with $pLFe^{48h}$ concentrations in unfiltered samples as the second filter pore size increases from 3 to 53 µm indicates that most of the $pLFe^{48h}$ in the upper 300 m is associated with particles in the 3–53 µm size range.

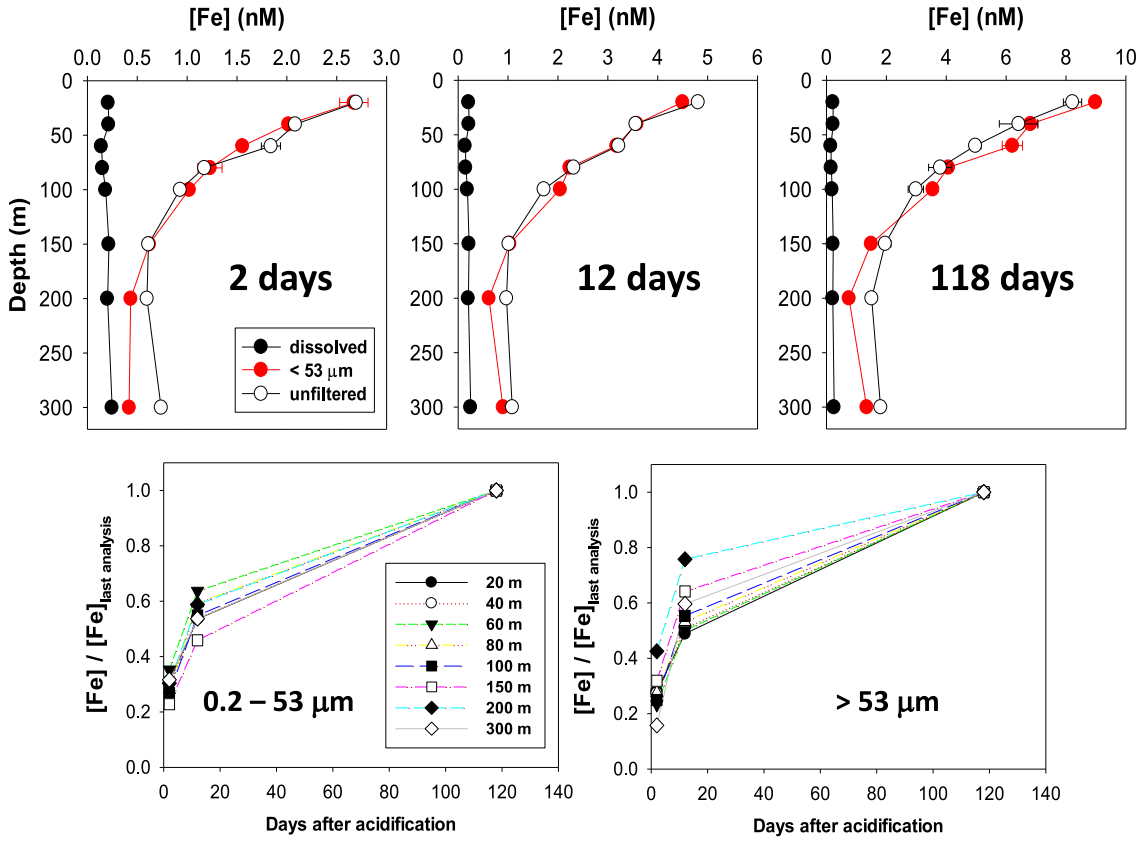

Figure 5. Top: vertical profiles of iron concentrations at location D of samples filtered by 0.2 µm (dFe), 53 µm and unfiltered acidified (pH 2.0) for 2, 12, and 118 days. Bottom: kinetics of iron leaching (normalized to the concentration on day 118) for the <53 µm (left) and unfiltered samples (right).

concentrations in the context of natural fertilization near South Georgia Island, which we will address in Section 4.7.

At location A, our dFe concentrations are largely consistent with previous findings from this sector of the Southern Ocean (Figure 6) (Klunder et al., 2011; Sieber et al., 2021). Specifically, all available dFe profiles exhibited similar trends, characterized by low surface concentrations and a linear increase with depth between 100 and 500 m. This pattern is typically attributed to a combination of surface uptake, remineralization at depth, advective fluxes, and increased solubility associated with the upwelling of low-oxygen waters. Sieber and collaborators reported lower dFe concentrations (0–0.3 nM less) between 300 and 500 m compared to our data, while Klunder and collaborators found intermediate values (Figure 6) (Klunder et al., 2011; Sieber et al., 2021). The high variability in dFe concentrations in this frontal zone has previously been attributed to fluctuations in the contribution of upwelled, low-oxygen UCDW to the upper layers (Puigcorbé et al., 2017; Sieber et al., 2021). The reducing potential of the upwelled UCDW, potentially stabilizing the more soluble Fe(II), is supported by elevated methylmercury concentrations observed down to 200 m exclusively at location A during our cruise (Canário et al., 2017).

4.2. Regional Homogeneity of Surface dFe Concentrations Along 52°S

Despite sampling at locations separated by thousands of kilometers, all dFe vertical profiles in the upper 300 m along the 52°S band were remarkably similar in both concentration and shape (Figures 2 and 7a). As a result, dFe standing stocks in the upper 100 m varied within a narrow two-fold range, from 10.8 to 21.2 µmol m^{-2} (Table 1). Our findings align closely with previous studies (see Section 4.1) and with two dFe profiles collected during the same cruise in bloom waters at 50°S 39°W, west of location D (Hoppe et al., 2017).

This regional consistency was observed despite pronounced variability in water masses properties, distance from dust sources, ML and euphotic layer depths, nutrient concentrations (Figure S1 in Supporting Information S1),

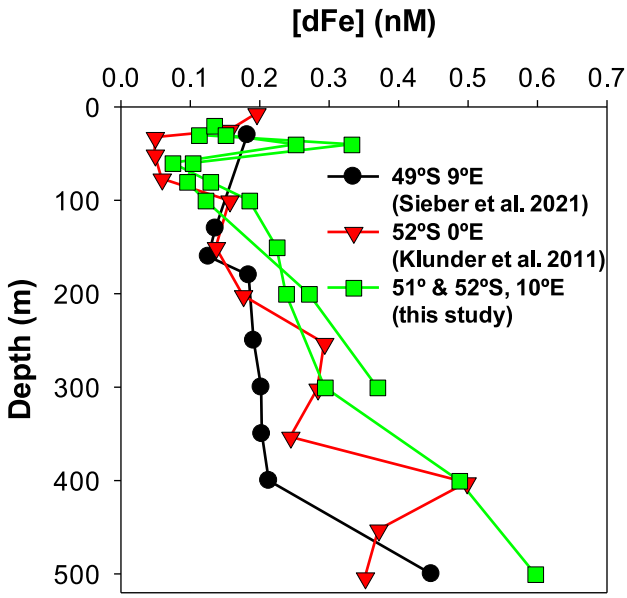

Figure 6. Vertical profiles of dissolved Fe concentrations at station A during this study are shown alongside data from previous cruises along the GEOTRACES GIPY04 transect for comparison.

temperature, biomass (Figures 1b and 1c), and biological community composition (Hoppe et al., 2017; Strass, Wolf-Gladrow, et al., 2017). Excluding location D, where iron dynamics were likely controlled by distinct processes (see Section 4.7), biomass, represented by Chl *a* and POC standing stocks in the upper 100 m, was significantly negatively correlated with dFe standing stocks ($r = -0.616$, $p = 0.043$, $n = 11$ for Chl *a* and $r = -0.602$, $p = 0.050$, $n = 11$ for POC) (Table 1).

At location C, dFe standing stocks remained consistent over a 3-week period. This stability persisted despite major biological and physical changes, including: (a) an approximate 50% decline in Chl *a* and POC standing stocks (Figure 2 and Table 1); (b) changes in the shape of Chl *a* profiles (Figures 1b and 1c); (c) sustained POC export at 100 m deep (see Section 4.4) (Roca-Martí et al., 2017); and (d) substantial physical variability, including ML warming, ML depth fluctuation (Figure 2), storms, and thermocline depth fluctuations (Strass, Leach, et al., 2017).

While trophic interactions in ocean ecosystems are typically described using a bottom-up framework, starting with the uptake of micronutrients such as iron, the observed negative correlation between dFe and biomass in this region suggests more intricate dynamics. The absence of a dominant biological or physical driver controlling dFe standing stocks and profile shapes points to the involvement of multiple potentially ubiquitous processes. We hypothesize that the stability of dFe standing stocks in the upper 100 m of the 52°S band results from a combination of: (a) rapid biological reutilization of remineralized particulate iron (discussed in Section 4.6); and (b) the widespread presence of a ubiquitous, non-bioavailable dFe fraction. This non-bioavailable fraction could consist of iron bound to organic ligands with limited bioavailability, inorganic nanoparticles, or a combination of both, either as separate entities or mixed organic and inorganic species (Gledhill & Buck, 2012). Non-bioavailable complexes may include ligands with very high stability constants for iron that do not promote iron reduction to more bioavailable Fe(II), as observed in some microbial siderophores (Barbeau et al., 2003). The non-bioavailable inorganic fraction may be comprised of aged iron oxyhydroxides or silicate-bound iron resistant to physical, chemical, and biological processing during their residence in the epipelagic layer (Revels et al., 2015).

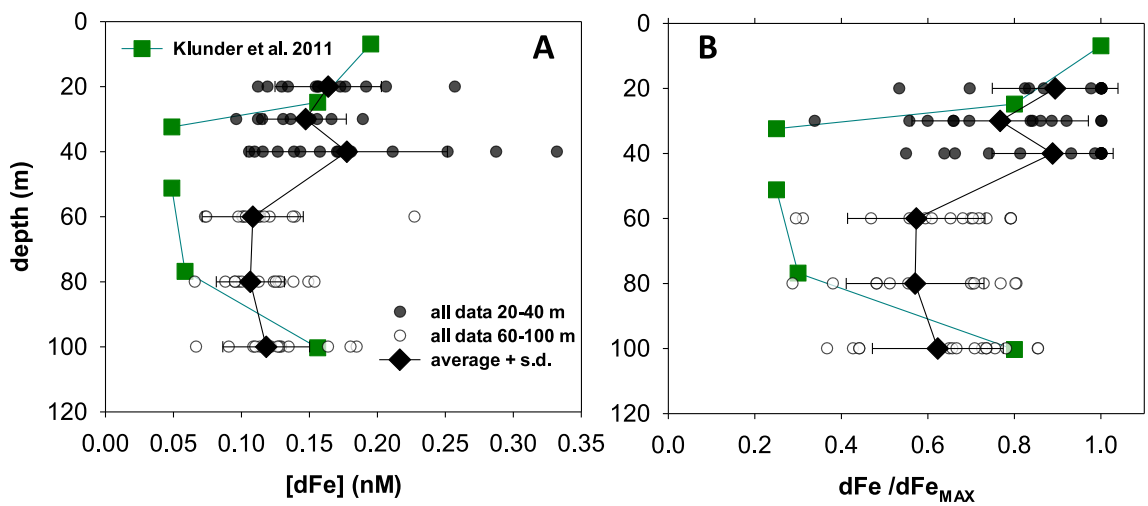

Figure 7. (a) Summary of dissolved Fe (dFe) concentrations in the upper 100 m measured during the ANT-XXVIII/3 cruise (circle symbols, all data from this cruise including Hoppe et al., 2017) and the ANT-XXIV/3 cruise (green squares, Klunder et al., 2011). Diamond symbols indicate depth-averaged dFe concentrations from the ANT-XXVIII/3 data set. (b) Same data as in panel (a), normalized to the maximum dFe concentration of each profile. Average normalized values are 0.85 ± 0.17 for the 20–40 m depth range and 0.63 ± 0.16 for the 60–100 m depth range.

In this scenario of rapid utilization of remineralized particulate Fe and ubiquitous presence of non-bioavailable dFe, biological activity would be sustained by more bioavailable iron fractions that cycle rapidly between the particulate and dissolved phases. Iron released during remineralization would be preferentially and rapidly taken up, escaping detection in the brief snapshot of oceanographic sampling. This interplay of processes likely explains the observed negative correlation between dFe standing stocks and biomass in this low dFe environment.

4.3. Generalized dFe Stratification in the Upper 100 m at 52°S

All dFe profiles in this study exhibited a previously unreported stratification within the upper 100 m (Figure 2). To statistically assess the consistency of this feature, we combined all profiles from the ANT-XXVIII/3 cruise, including those reported by Hoppe et al., and added the data set from Klunder et al. (Figure 7) (Hoppe et al., 2017; Klunder et al., 2011). Because absolute dFe concentrations varied substantially between profiles (Figure 7a) we normalized each profile to its respective maximum dFe concentrations (Figure 7b). This approach minimizes the influence of station-to-station variability in absolute dFe levels and highlights consistent vertical patterns across profiles. The resulting normalized concentrations confirmed that dFe in the 20–40 m layer (average of 0.85 ± 0.17, $n = 45$) was significantly higher than that in the 60–100 m layer (average of 0.63 ± 0.16, $n = 41$), as determined by a Mann-Whitney rank-sum test ($T = 2{,}396.5$, $p < 0.001$), appropriate given the non-normal distribution of the normalized dFe data.

Notably, the upper boundary of lower dFe concentrations at 60 m was just beneath the euphotic zone (54 ± 8 m at location A and 30 ± 8 m at locations B and C) (Cheah et al., 2017; Hoppe et al., 2017) and was independent of the ML depth, which ranged from 55 to 90 m at location A and from 36 to 89 m at location C (Strass, Leach, et al., 2017). The lower boundary of the dFe minimum at 100 m approximately coincided with the variable vertical extent of Chl *a* (Figure 1) and with steep increases in nitrate and phosphate (Figure S1 in Supporting Information S1). At location B, despite low biomass and a ML depth of 71 m, dFe exhibited the same stratification.

If ML depth variability at location C (Figure 2) had dominated dFe dynamics, entrainment of dFe-rich deeper waters would have increased dFe concentrations in the 60–100 m range. Paradoxically, the dFe minimum lies just below the euphotic layer, where dFe uptake by primary producers is low, implying limited biological removal, while remineralization, which releases dFe, is intense, as evidenced by the very low POC export efficiency at 100 m (Roca-Martí et al., 2017). The persistence of the subsurface dFe minimum across contrasting hydrographic and biological conditions suggests the influence of other overlapping general processes, the relative importance of which we cannot evaluate. First, if our hypothesis of the presence of a ubiquitous fraction of non-bioavailable dFe is correct, its concentration may be lower within this layer. Second, although dFe uptake by phytoplankton likely declines rapidly as the biomass decreases with depth, microbial uptake by heterotrophic bacteria may increase at depths of intense remineralization. Such microbial activity may contribute to local dFe depletion (Obernosterer et al., 2015). Conversely, dFe scarcity in the 60–100 m range could limit microbial remineralization itself, as proposed for deeper waters of the Pacific Ocean (Li et al., 2024). Third, depth-dependent aggregation or authigenic Fe formation may also remove dFe through particle scavenging at different rates as a function of depth (explored in Section 4.5). Finally, the absence of photochemical reduction of Fe(III) to the more soluble Fe(II) below the euphotic zone may reduce iron solubility. At the surface, the stability of freshly produced Fe(II) is enhanced in the cold waters of the Southern Ocean (Croot & Laan, 2002; Laglera et al., 2022). Dissolved Fe(II) vertical gradients of up to 0.1 nM between 30 and 50 m have been observed in Southern Ocean bloom waters during iron fertilization experiments (Croot & Laan, 2002; Laglera et al., 2022).

Importantly, the sharp inverse gradient at the top of the dFe minimum likely restricts vertical diffusive flux into the euphotic zone, reinforcing the need to identify the mechanisms maintaining this unexpected stratification.

4.4. The Role of $pLFe^{48h}$ in Iron Cycling

To investigate the magnitude and nature of iron remineralization, we acidified unfiltered seawater to pH 2.0 for 48 hr, following the protocol used during the LOHAFEX iron fertilization experiment (Laglera et al., 2017). This approach was designed to target particulate iron forms that are readily remineralized and potentially available to sustain primary productivity, while excluding iron within viable cells and mineral forms. It is important to note that although applied to particle-containing samples, electrochemical detection ensures that only solubilized iron is measured. The method previously proved effective in accurately estimating iron in copepod (*Calanus simillimus*) fecal pellets without measuring iron from intact phytoplankton (Laglera et al., 2017). The efficiency of

mild acid leaching depends on the zooplankton species releasing the pellets: copepods' particle-grinding feeding strategy before ingestion results in apparent complete Fe recovery, whereas salps' filtration-based feeding leaves many ingested cells intact after gut transit (Caron et al., 1989), yielding in *S. thompsoni* fecal pellets only ~10% recovery (Cabanes et al., 2017). Overall, mild acid leaching selectively targets iron in zooplankton fecal material, with efficiency varying by the feeding strategy.

Thus, we hypothesize that our analytical protocol effectively measures iron in zooplankton fecal material, with its efficiency dependent on the dominant zooplankton group, and other detrital particles. It likely solubilizes fresh iron oxyhydroxides but recovers only a minor portion of aged oxyhydroxides or dust-derived particles (Raiswell, 2011; Shi et al., 2011).

Notably, our protocol is characterized by intermediate extraction relative to GEOTRACES protocols for the determination of "total" and "labile" particulate iron (Aguilar-Islas et al., 2024). Total particulate iron is determined after prolonged acidification at pH 1.7 or below and microwave digestion, while "labile" particulate iron is determined by Berger's method, which involves exposing filters to a mixture of acetic acid and hydroxylamine hydrochloride at pH 2 with a brief heating step (Berger et al., 2008). However, for practical reasons, many studies apply a simplified version using acetic acid at room temperature (Planquette et al., 2009; Schlosser et al., 2018). Interestingly, our location D is situated a few miles from station 15/16# sampled in January 2011 by Schlosser et al., 2018. At that site, they reported in the upper 150 m considerably higher dFe concentrations (range 0.73–1.2 nM), slightly lower labile concentrations (range 0.43–0.90 nM; $n = 3$) and total particulate Fe concentrations ranging from 4.7 to 28 nM, substantially greater than the concentrations we recovered after 118 days at pH 2.0 (Schlosser et al., 2018). Direct comparison of concentrations from different treatments is challenging, as diverse leaching methods may target distinct iron pools and yield varying recoveries even from the same particle type; the Berger method has yet to be tested on distinct biological particles.

We used $pLFe^{48h}$ standing stocks in the upper 100 m to gain insights into iron cycling in the region. At locations A to C, $pLFe^{48h}$ standing stocks (18–77 μmol Fe m^{-2}) generally exceeded dFe stocks and showed no significant correlation with them ($r = -0.383$; $p = 0.245$; $n = 11$) (Table 1). While dFe was negatively correlated to Chl *a* and POC, $pLFe^{48h}$ showed positive correlations, though not statistically significant ($r = +0.530$; $p = 0.093$; $n = 11$ for Chl *a* and $r = +0.483$; $p = 0.132$; $n = 11$ for POC). However, excluding $pLFe^{48h}$ concentrations at 20 m (where high scattered values potentially indicate ship contamination or less likely aeolian inputs, Figure 3), both positive correlations became significant ($r = +0.626$, $p = 0.039$, $n = 11$ for Chl *a* and $r = +0.661$, $p = 0.027$, $n = 11$ for POC). Remarkably, at location B, $pLFe^{48h}$ showed near complete depletion in the upper 100 m (Figure 4 and Table 1). This pattern suggests that $pLFe^{48h}$ plays a key role in the distribution, build up, and dynamics of biomass in this region.

4.5. Insights Into the Nature of $pLFe^{48h}$ From Size Fractionated Samples

Size-fractionated filtration was used to identify particles contributing to $pLFe^{48h}$, though only three size classes could be processed due to sampling and processing constraints. Initial results showed minimal $pLFe^{48h}$ in the 0.2–0.4 and 0.2–3 μm ranges (Figure 4), prompting an increase in pore size for subsequent sampling. Despite not applying all size fractions throughout the entire time series, we consider henceforth that the lack of signal in smaller fractions supports the conclusion that most $pLFe^{48h}$ was absent in particles <3 μm during the bloom decay, with only minor concentrations detected between 80 and 100 m (Figure 4 and Figure S3 in Supporting Information S1). This absence suggests that: (a) cells in the 0.2–3 μm size range (pico and part of nanoplankton) did not significantly contribute to $pLFe^{48h}$, aligning with previous culture-based observations (Laglera et al., 2017); and (b) the formation of authigenic iron oxyhydroxides was limited, as such species are expected to nucleate and grow across a size continuum before sinking. The apparent lack of authigenic iron in areas of high biological activity supports model predictions for the Southern Ocean (Tagliabue et al., 2023), but our results suggest this process may be even more suppressed than anticipated, warranting further study in other high biomass regions.

A relevant comparison can be made with a previous study in the Amundsen Sea, where size-fractionated particulate iron (0.45–5 μm and >5 μm) was determined using strong acid digestion (Planquette et al., 2013). Particulate Fe concentrations were substantially higher than the $pLFe^{48h}$ concentrations reported in this study, particularly in blooming coastal polynyas. However, Fe:Al and Fe:P ratios indicated that only 2%–25% of particulate iron offshore in both fractions was biogenic, and in coastal polynyas the overwhelming lithogenic

material effectively buried the biogenic contribution, making it negligible despite the abundant presence of biological particles. In contrast, our lower $pLFe^{48h}$ concentrations likely reflect a smaller but more biologically available and actively recycled iron pool, underscoring the utility of gentle leaching protocols for isolating iron associated with biological particles.

At locations C after day 16 and D, most $pLFe^{48h}$ was found in the <53 μm size range (Figures 4 and 5 and Figure S3 in Supporting Information S1). The contribution of "fast" sinking $pLFe^{48h}$ (>53 μm) was minor except during two episodes: day 16 at location C and below 150 m at location D, where the >53 μm fraction accounted for up to 40% of $pLFe^{48h}$. The cause of these anomalies remains unclear. Although sediment trap data at location C showed no marked changes in Chl *a* concentrations and POC export on day 16 (Table 1) (Roca-Martí et al., 2017), the percentage of "fast" sinking $pLFe^{48h}$ was apparently higher in the upper 100 m, indicative of biological processes. This may indicate POC export pulses (Smetacek et al., 2012), a feature previously documented in Southern Ocean blooms using high-resolution glider data (Henson et al., 2023). We hypothesize that spatial and temporal variability in zooplankton distribution and activity may drive the pulsed export of iron and POC (Smetacek et al., 2004).

Between 80 and 100 m at location C, we consistently detected small amounts of $pLFe^{48h}$ in the 0.2–3 μm size range (Figure 4 and Figure S3 in Supporting Information S1). This layer was characterized by low dFe and $pLFe^{48h}$ concentrations, reduced irradiance, variable Chl *a* concentrations (Figure 1), and steep nutrient vertical gradients (Figure S1 in Supporting Information S1). While the combination of these features might promote the stabilization of iron aggregates, possibly partly composed of mixed mineral and organic species (Boye et al., 2010), the narrow vertical confinement of this fraction is intriguing. We hypothesize that possible explanations include constrained microbial activity due to low dFe availability (Li et al., 2024), reduced zooplankton grazing pressure, or localized reduction of phagotrophy of fresh aggregates by small flagellates (Barbeau et al., 1996; Maranger et al., 1998). This depth represents a transitional zone for vertically migrating zooplankton, lying between nighttime surface residency and deeper daytime habitats (Mazzocchi et al., 2009; Pollard et al., 2002).

4.6. Estimation of the Contribution of Biological Processes to Iron Fluxes Between Dissolved and Particulate Phases

Transfers of organic carbon in the ocean are closely linked to iron fluxes, with trophic and remineralization altering iron speciation and partitioning between particulate and dissolved pools (Boyd et al., 2010; Laglera et al., 2020; Sato et al., 2009). In this section, we estimate the magnitude of biologically driven iron cycling during our study by combining published carbon inventories and fluxes obtained during our cruise (Cheah et al., 2017) with Fe:C stoichiometries reported for Southern Ocean phytoplankton communities (Hopkinson et al., 2013; Martiny et al., 2013; Twining & Baines, 2013).

The Fe:C ratio of biological particles varies with community composition, dFe availability, temperature, and other environmental factors (Sunda & Huntsman, 1995). To estimate the biological reservoir of iron and daily iron assimilation by primary producers, we used POC and net primary production (NPP) data (Table 1) in combination with a Fe:C ratio of 15 μmol mol^{-1}. This value was derived from Fe:P ratios for diatom-dominated communities and converted using the characteristic C:P ratio of high-latitude Southern Ocean waters (Martiny et al., 2013; Twining & Baines, 2013). However, as particles sink, respiration and remineralization by microbes and zooplankton substantially modify Fe:C stoichiometries, making surface-derived ratios unreliable for estimating iron export (defined as the downward flux at 100 m). While sinking dead phytoplankton may retain Fe:C ratios similar to those of living cells, zooplankton-mediated export can be substantially enriched in iron. Zooplankton do not accumulate significant amounts of iron themselves (Ratnarajah & Bowie, 2016), but their fecal material is enriched in iron relative to their food, an enrichment that has been estimated to average a factor of 9.0 (Le Mézo & Galbraith, 2021). There are currently no measurements of heterogeneous and loosely aggregated constituents of marine snow subjected to microbial degradation. Therefore, to bracket uncertainty calculating biological iron export, we apply Fe:C ratios of 15 and 140 μmol mol^{-1}, representing export dominated by, respectively: dead diatoms cells keeping their Fe:C stoichiometry and fecal material.

We estimated that the biological standing stocks (Fe^{bio}), calculated from POC in our area of study, amounted to 11.5 μmol Fe m^{-2} at location A, 8 μmol Fe m^{-2} at location B, and 13–32 μmol Fe m^{-2} at location C. For comparison, $pLFe^{48h}$ standing stocks were 2.4 ± 1.1 times higher. On average, the integrated daily NPP

represented about 10% of the POC standing stock, corresponding to a turnover time of approximately 10 days (excluding location B, where it was only 2%). The daily biological demand of iron was 1.1 μmol Fe m^{-2} d^{-1} at location A, 0.2 μmol Fe m^{-2} d^{-1} at location B and ranged from 1 to 3.5 μmol Fe m^{-2} d^{-1} at location C. These values suggest a rapid biological cycling of iron in the upper ocean, where 8%, <1%, and 19% of the dFe standing stock was turned over daily to sustain biological productivity at the three locations.

Despite uncertainties, it is evident that dFe standing stocks must be replenished every few days to sustain the biomass measured at location C for over many weeks. External iron inputs in this remote region from lateral and vertical advection and diffusion fluxes and from dust dissolution are expected to be low, possibly all combined below 0.1 μmol Fe m^{-2} d^{-1} (Cabanes et al., 2017). Average POC exports obtained from ^{234}Th measurements were 0.029 and 0.026 mol C m^{-2} d^{-1} at locations A and C, respectively (Puigcorbé et al., 2017; Roca-Martí et al., 2017). Whereas at location A this represents an important daily loss of 40% of NPP (about 4% of the POC standing stock) (Puigcorbé et al., 2017), at location C this export represents 16% of NPP (about 1.7% of the POC standing stock) (Roca-Martí et al., 2017).

If we apply the aforementioned Fe:C ratios for POC export, we may estimate that at location A, 0.44–4.1 μmol Fe m^{-2} d^{-1} are lost daily. This range, whose upper limit is equivalent to 30% of the dFe standing stock, underlines our need to better constrain the trace element stoichiometry of the material exported from the ML. A downward flux of material with a heavy presence of zooplankton fecal pellets has the potential to deplete ML Fe standing stocks in a few days.

At location B, there was no iron limitation since the daily iron requirement was <1% of the dFe standing stock and nutrients were abundant (Hoppe et al., 2017). Very low Chl *a* concentrations were probably related to the abundance of salps in the area. We further hypothesize that low $pLFe^{48h}$ concentrations were the result of efficient biomass removal through filtration by salps. This process would result in fecal pellets containing numerous viable cells that are less susceptible to leaching under our protocol.

We can reach a better understanding of how iron cycles from the time series obtained at location C (summary in Figure 8) characterized by an open ocean bloom that lasted for 3 months in its final stage of slow decline (Hoppe et al., 2017). Negative correlation coefficients of −0.91, −0.85, and −0.88 for the regression of Chl *a*, POC, and NPP with respect to time (Pearson regressions; $p < 0.05$), confirmed the declining trend of the bloom (Hoppe et al., 2017) with losses of 40%–50% over the 18 days of the experiment. The apparent loss of pFe^{bio} and $pLFe^{48h}$ (not statistically significant; $p > 0.05$) was 12 and 30 μmol Fe m^{-2}, respectively (Table 1). Estimated iron export ranged from 0.4 to 3.6 μmol Fe m^{-2} d^{-1} corresponding to a cumulative loss of 7–66 μmol Fe m^{-2} over 18 days, values consistent with the combined loss of 43 μmol Fe m^{-2} from the pFe^{bio} and $pLFe^{48h}$ standing stocks. These estimates indicate that biological iron export can account for the observed decline in these particulate iron fractions in the upper 100 m during the study period. However, the average daily removal of nearly 20% of the dissolved Fe standing stock, which remained stable over 18 days, suggests that NPP was sustained by efficient local recycling in the surface layer. Figure 8 illustrates the main biological iron recycling pathways inferred from our estimates (see also Laglera et al., 2017 for more details).

A simple calculation can illustrate the relevance of POC composition and Fe:C ratios in iron export. Although data for other zooplankton groups are unfortunately lacking, salp fecal pellet standing stocks were measured, and associated carbon and iron export fluxes were estimated at Station C (Cabanes et al., 2017; Iversen et al., 2017). Despite their high Fe:C ratio, salps contributed minimally to iron export at location C, with only ∼0.2% of daily NPP being transferred into fecal pellets (Iversen et al., 2017). If the POC export had been comprised exclusively of salp fecal pellets, due to their high Fe:C ratio, the daily iron export would have been approximately 6 μmol Fe m^{-2}, which would have consumed surface Fe standing stocks within 12 days (Cabanes et al., 2017).

To explain the stability of dFe profiles, we propose that remineralized $pLFe^{48h}$ is significantly more bioavailable than a ubiquitous non-bioavailable dFe fraction. This labile particulate iron is likely remineralized directly within the ML, providing an immediate and localized source of dFe. During remineralization, cellular contents may release photosensitive ligands that facilitate the in situ formation of highly bioavailable Fe(II) (Laglera et al., 2020, 2022). The rapid reutilization of this iron pool, supported by the low export of NPP and the decline in POC standing stocks, may occur on timescales comparable to biological uptake (a few hours) (Shaked et al., 2020). This fast recycling could explain the weak correlation between $pLFe^{48h}$ and ambient dFe concentrations. Overall, these findings highlight the importance of timescale mismatches in trace metal cycling: external

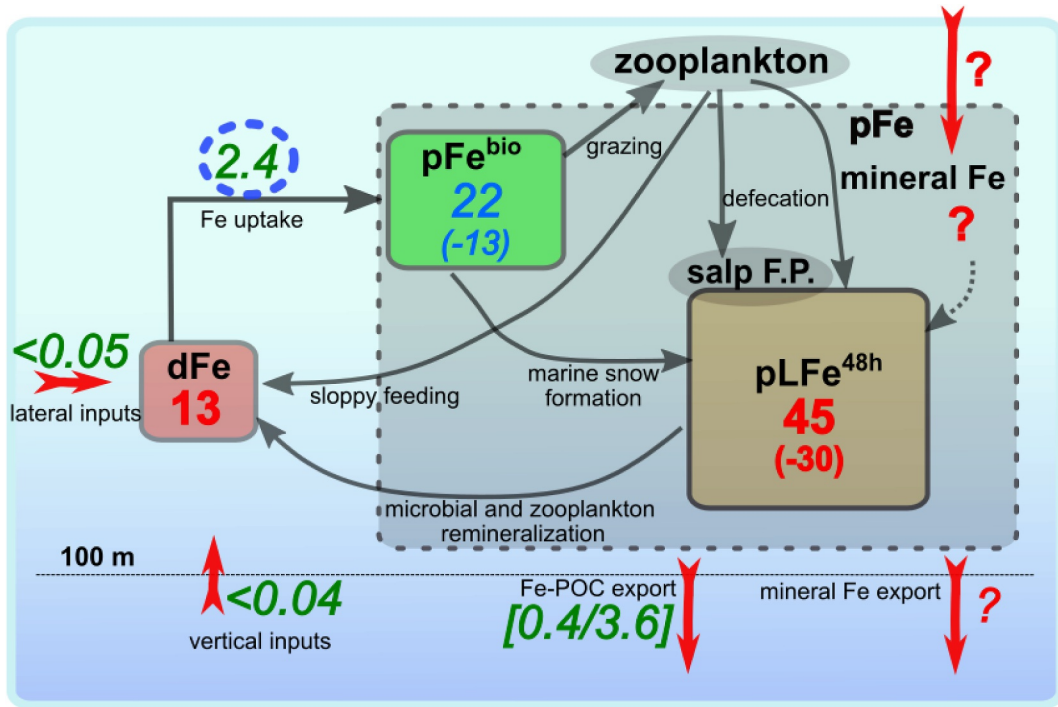

Figure 8. Major iron standing stocks and fluxes at location C during the ANT-XXVIII/3 cruise. Boxes represent standing stocks in the upper 100 m. Red numbers indicate the two iron standing stocks measured in this study: dFe refers to dissolved iron (<0.2 μm) and $pLFe^{48h}$ represents leachable particulate iron (>0.2 μm) after 48 hr at pH 2.0. The blue number in the green box indicates the estimation of biological particulate iron (pFe^{bio}), calculated from average POC standing stocks using an Fe:C stoichiometry of 15 μmol mol^{-1}. Negative numbers in the pFe^{bio} and $pLFe^{48h}$ boxes are the decrease of standing stocks from our arrival to day 18 calculated from least square linear regressions of pFe^{bio} and $pLFe^{48h}$ with time. Green numbers denote fluxes; inputs to the upper 100 m are based on calculations from de Jong et al. (2012); Fe uptake is calculated from NPP multiplied by Fe:C of 15 μmol mol^{-1} and Fe-POC export is estimated from POC export (Puigcorbé et al., 2017; Roca-Martí et al., 2017) multiplied by Fe:C ratios 15 and 140 μmol mol^{-1}. Black arrows represent hypothesized major iron cycling pathways in the upper 100 m. Gray boxes for mineral iron and salp fecal pellets overlap with the $pLFe^{48h}$, reflecting that a portion of these pools is likely labile under our leaching protocol.

sources, such as atmospheric or deep-water inputs, often require slow dissolution and vertical mixing, potentially making them less effective at meeting the rapid iron demand of surface phytoplankton communities.

Overall, our proposed fluxes and processes shed light on the mechanisms that extend the life of open ocean blooms (Figure 8). After winter replenishment or external inputs, biological communities may thrive under low dFe concentrations if there is a storage of rapidly recyclable iron in "slow" sinking particles under grazing conditions that reduce Fe export. We estimate that the daily recycling of approximately 5% of the $pLFe^{48h}$ standing stock may be sufficient to sustain a diatom bloom with Chl *a* concentrations exceeding 1.5 mg m^{-3} for several weeks in the absence of external iron inputs. This recycling is likely driven by a combination of biological processes, including grazing, defecation, and the breakdown of fecal pellets through coprorhexy (fragmentation) and coprochaly (peeling) that reduce their size and therefore sinking velocity. These processes, together with bacterial remineralization and sloppy feeding on cells and fecal material, continuously generate bioavailable iron from the $pLFe^{48h}$ pool. Collectively, they form an efficient internal loop that maintains iron availability in surface waters (Iversen & Poulsen, 2007; Poulsen & Iversen, 2008). Efficient biological remineralization of iron by processes associated with grazing was used to interpret bloom resilience after ocean iron fertilizations (Bowie et al., 2001; Laglera et al., 2017) and is concurrent with the interpretation of processes in the surface Southern Ocean used in recent models (Tagliabue et al., 2017).

4.7. South Georgia Island as a Significant Source of Aeolian Iron

The region within the Georgia Basin including location D, situated on the edge of the South Georgia's north-western shelf, exhibits dynamism and variability of physical conditions. This dynamism is attributed to the

retroflection of the Southern Antarctic Circumpolar Current Front (SACCF), which follows an anticyclonic route around the island before resuming its eastbound trajectory (Meredith et al., 2003).

The relative contribution of the different sources of bioavailable iron that sustain recurring phytoplankton blooms in the area remains poorly characterized (Borrione & Schlitzer, 2013; Hoppe et al., 2017). Prior cruises north of South Georgia recorded significant seasonal and spatial variability in F_V/F_M ratios and dFe concentrations, with dFe offshore concentrations ranging from <0.03 to 6 nM (Nielsdóttir et al., 2012; Schlosser et al., 2018). These studies proposed that iron fueling blooms in the region are mainly supplied via vertical transport from the island's shelf by the action of the SACCF, combined with extended residence times due to trophic recycling and biological uptake (Nielsdóttir et al., 2012; Schlosser et al., 2018). Here, we propose an additional mechanism contributing to iron cycling in this region.

At location D, the biogeochemical conditions differed from those at the other locations; Chl *a* concentrations (up to 1.2 mg m^{-3}) decreased nearly exponentially down to 100 m, the surface F_V/F_M ratio was 0.5 (indicative of biological iron replenishment) and a shallower ML depth (Figure 2 and Figure S5 in Supporting Information S1). Although dFe concentrations and vertical profiles were similar to those of the other locations (Figure 2), $pLFe^{48h}$ concentrations were notably higher and exhibited a well-defined exponential profile mainly comprising "slow" sinking particles. This profile shape and high concentrations suggest that aeolian deposition is on a timescale shorter than that of ML homogenization, likely indicating a nearby origin.

The relative leaching kinetics of particulate iron were consistent across samples down to 300 m when the acidification period at pH 2.0 was extended for months, pointing to a common source. Comparison with experiments on known particle types under the same pH rules out significant contributions to pLFe from copepod fecal pellets (which would have been fully leached by day 2), or viable phytoplankton cells (which retain most of their iron for several days) (Laglera et al., 2017) and organic-iron complexes (which dissociate within hours) (Laglera et al., 2013). Our observed leaching time scales, on the order of months, are consistent with those reported for dust samples derived from riverbed soils, collected during a dust storm and resuspended in water at pH 2 (Shi et al., 2011). Periodic ferrozine analysis of 0.2 μm filtered subsamples yielded leaching kinetics consistent with our observations.

In contrast, Schlosser and co-authors applied a more aggressive leaching protocol, nearly 1 year at pH 1.7, to unfiltered samples from north of South Georgia, extracting more refractory iron, including most of the mineral iron (Schlosser et al., 2018). Their results showed highly variable pLFe concentrations (1–128 nM, equivalent to 10% to 1,500% of the maximum $pLFe^{48h}$ we observed) and diversely shaped vertical profiles across nine stations (Schlosser et al., 2018). At many shelf stations, pLFe increased with depth, interpreted as evidence of shelf resuspension. Near our location D, they reported uniform pLFe concentrations of ∼20 nM in the upper 75 m, decreasing to 2 nM below, interpreted as efficient mixing of lithogenic and authigenic iron. Only at one shallow station located in the vicinity of King Edward Point, they observed an exponential pLFe decrease from 107 to 5 nM in the upper 150 m (Schlosser et al., 2018), resembling our $pLFe^{48h}$ profile at location D.

Given the limited dust inputs from Patagonia at location D (Chance et al., 2015; Tagliabue et al., 2017), alternative sources might explain the distinct profile observed. The island has an elongated profile, stretching 170 km from NW to SE, with a mountainous central ridge rising to 2,935 m and covering two-thirds of the island's length, permanently covered in snow. Prevailing westerly winds blow perpendicular to the orographic axis, facilitating the occurrence of robust Föhn winds and consequently the resuspension of snow and ice, averaging 7.2 Föhn events per month (Bannister & King, 2015). We hypothesize that material accompanying resuspended snow covering South Georgia Island serves as a key source of particulate iron to the waters north of the island when westerly winds prevail. The leeward position at location D with respect to South Georgia, and the perpendicular orientation of the island to dominant westerly winds suggest that strong winds passing over the island's central peaks could entrain and transport snow and associated particles into adjacent waters (Figure S3 in Supporting Information S1). While similar mechanisms have been considered for aeolian iron transport from Antarctic ice sheets (de Jong et al., 2013) and for resuspension from island shelves (Blain et al., 2007; Planquette et al., 2007), the potential contribution of aeolian iron transport from island ice cover has not yet been explored.

This flux, modulated by wind field intensity, direction, and the island's steep orography, likely acts alongside other regional iron sources. The slow solubilization of a small fraction of this aeolian particulate iron during the extended residence time in the upper 100 m of "slow" sinking material may alleviate iron stress at location D. The

low dFe concentrations observed likely reflect the slower solubilization rates relative to the faster bioassimilation rate. In the bloom observed during the Eddy Pump cruise at 39°W, where Chl *a* concentrations were slightly lower (standing stocks at 52 and 53°S of 68 and 80 mg Chl *a* m^{-2}, respectively), the NPP was estimated at 116 mmol C m^{-2} d^{-1} (Hoppe et al., 2017), corresponding to an estimation of the iron demand of 1.7 μmol Fe m^{-2} d^{-1} (using again a Fe:C ratio of 15 μmol mol^{-1}). This daily iron demand represents 4%–25% of the dFe standing stock, but only 0.5%–2.7% of the $pLFe^{48h}$ standing stock. For comparison, Schlosser and coauthors estimated the combined contribution of dust solubilization, diapycnal mixing and lateral advection in this region to be over an order of magnitude smaller, at 0.11 μmol dFe m^{-2} d^{-1} (Schlosser et al., 2018).

Below 150 m, a significant fraction of $pLFe^{48h}$ was found in "fast" sinking particles. This likely reflects in situ aggregation of the same inorganic material found in the upper 150 m, rather than contributions from biological material, given the consistent leaching kinetics observed down to 300 m.

In the absence of negative vertical gradients in either dFe or $pLFe^{48h}$, and at a site with a water column depth of 1,200 m, we argue that only the combined effect of the generalized lateral advection driven by the SACC and iron fluxes from aeolian inputs sourced from the island can account for the observed $pLFe^{48h}$ profile at location D.

5. Conclusions

This study provides new insights into upper-ocean iron cycling in the Atlantic sector of the Southern Ocean based on observations from multiple locations and a time-resolved series during bloom development. Together, these measurements show how biologically mediated processes influence the partitioning, retention, and export of iron in this climatically important region.

Our results showed that dFe concentration was a poor predictor of biomass, whereas in contrast, $pLFe^{48h}$ was strongly and positively correlated with biomass, suggesting that the rapid remineralization of a small fraction of this labile particulate fraction plays a key role in supplying bioavailable iron during blooms. Across all stations, a consistent dFe minimum was observed at 80–100 m, independent of local physical conditions, biomass, $pLFe^{48h}$ standing stocks, or ML depth. Its alignment with the permanent Chl *a* and macronutrient gradient indicates that it is related to remineralization processes at this depth. This finding underscores the importance of accounting for the differing timescales of biological uptake, particle recycling, and abiotic supply processes when interpreting trace element distributions in the upper ocean.

Size-fractionation experiments revealed that the aggregation of fresh inorganic particles was restricted, and the formation of sinking authigenic iron was negligible, with only trace amounts confined to the narrow depth interval between 80 and 100 m. The particle size spectrum was dominated by the "slow" sinking 3–53 μm fraction, while "fast" sinking particles were relatively scarce and only important during a single sampling event. This partitioning effectively extended the residence time of $pLFe^{48h}$ in the ML, enabling sustained recycling and bioavailability of iron over multi-week timescales.

Our observations at the north of the South Georgia station suggest that particulate Fe supplied by wind-blown snow from island ice covers represents a previously disregarded and spatially variable iron source in this region, potentially contributing to persistent productivity hotspots.

The performance of our mild extraction method emphasizes the need to develop new extraction and fractionation protocols capable of resolving the distinct particulate pools and processes that govern trace element residence times and reactivity in the upper ocean. In this regard, direct electrochemical methods offer analytical advantages, enabling selective measurement of solubilized fractions after simple acidification protocols while being unaffected by refractory particles remaining in suspension. Overall, this study underlines the importance of monitoring trace element speciation and fractionation over extended periods within the same water mass, as the rapid evolution and variability we observed cannot be adequately captured by traditional transect-based sampling.

Conflict of Interest

The authors declare no conflicts of interest relevant to this study.

Availability Statement

Map in Figure 1a was produced using Ocean Data View. Figures and statistics were generated with SigmaPlot Software (SigmaPlot 12.0, Systat Software, Inc.). All data referred in the manuscript are publicly available from the PANGAEA open repository (www.pangaea.de). Physical variables are available via https://doi.pangaea.de/10.1594/PANGAEA.866935 (Strass, Leach, et al., 2017). Chl *a*, primary productivity and photosynthetic data are available via https://doi.org/10.1594/PANGAEA.878248 and https://doi.org/10.1594/PANGAEA.878246 (Cheah et al., 2017; Hoppe et al., 2017). Nutrient data are available via https://doi.org/10.1594/PANGAEA.878249 (Hoppe et al., 2017). Dissolved and particulate iron concentrations measured during the cruise at locations A, B and C are available via https://doi.pangaea.de/10.1594/PANGAEA.951782 (Laglera et al., 2025a). Dissolved, particulate iron concentrations and iron leaching kinetics at location D north of South Georgia are available via https://doi.pangaea.de/10.1594/PANGAEA.951902 (Laglera et al., 2025b).

Acknowledgments
The authors are grateful to the captain Uwe Pahl and crew of R/V Polarstern, and the scientists on board for their assistance during the cruise. This study received financial support from the MINECO of Spain (Grant CGL2010-11846-E) and MCIN/AEI/10.13039/501100011033/10.13039/501100011033 and FEDER, UE (project PID2023-148860OB-I00).

References

Aguilar-Islas, A. M., Bridgestock, L., Bundy, R. M., Conway, T. M., Hayes, C. T., Heimbürger, L. E., et al. (2024). Sampling and sample-handling protocols for GEOTRACES cruises, Version 4.0.

Anderson, R. F. (2020). GEOTRACES: Accelerating research on the marine biogeochemical cycles of trace elements and their isotopes. *Annual Review of Marine Science*, *12*(1), 49–85. https://doi.org/10.1146/annurev-marine-010318-095123

Bannister, D., & King, J. (2015). Föhn winds on South Georgia and their impact on regional climate. *Weather*, *70*(11), 324–329. https://doi.org/10.1002/wea.2548

Barbeau, K., Moffett, J. W., Caron, D. A., Croot, P. L., & Erdner, D. L. (1996). Role of protozoan grazing in relieving iron limitation of phytoplankton. *Nature*, *380*(6569), 61–64. https://doi.org/10.1038/380061a0

Barbeau, K., Rue, E. L., Trick, C. G., Bruland, K. W., & Butler, A. (2003). Photochemical reactivity of siderophores produced by marine heterotrophic bacteria and cyanobacteria based on characteristic Fe(III) binding groups. *Limnology & Oceanography*, *48*(3), 1069–1078. https://doi.org/10.4319/lo.2003.48.3.1069

Berger, C. J., Lippiatt, S. M., Lawrence, M. G., & Bruland, K. W. (2008). Application of a chemical leach technique for estimating labile particulate aluminum, iron, and manganese in the Columbia River plume and coastal waters off Oregon and Washington. *Journal of Geophysical Research*, *113*(C2). https://doi.org/10.1029/2007jc004703

Blain, S., Quéguiner, B., Armand, L., Belviso, S., Bombled, B., Bopp, L., et al. (2007). Effect of natural iron fertilization on carbon sequestration in the Southern Ocean. *Nature*, *446*(7139), 1070–1074. https://doi.org/10.1038/nature05700

Borrione, I., & Schlitzer, R. (2013). Distribution and recurrence of phytoplankton blooms around South Georgia, Southern Ocean. *Biogeosciences*, *10*(1), 217–231. https://doi.org/10.5194/bg-10-217-2013

Bowie, A. R., Maldonado, M. T., Frew, R. D., Croot, P. L., Achterberg, E. P., Mantoura, R. F. C., et al. (2001). The fate of added iron during a mesoscale fertilisation experiment in the Southern Ocean. *Deep-Sea Research Part II Topical Studies in Oceanography*, *48*(11–12), 2703–2743. https://doi.org/10.1016/S0967-0645(01)00015-7

Boyd, P. W., Ibisanmi, E., Sander, S. G., Hunter, K. A., & Jackson, G. A. (2010). Remineralization of upper ocean particles: Implications for iron biogeochemistry. *Limnology & Oceanography*, *55*(3), 1271–1288. https://doi.org/10.4319/lo.2010.55.3.1271

Boyd, P. W., Law, C. S., Hutchins, D. A., Abraham, E. R., Croot, P. L., Ellwood, M., et al. (2005). FeCycle: Attempting an iron biogeochemical budget from a mesoscale SF6 tracer experiment in unperturbed low iron waters. *Global Biogeochemical Cycles*, *19*(4). https://doi.org/10.1029/2005GB002494

Boye, M., Nishioka, J., Croot, P., Laan, P., Timmermans, K. R., Strass, V. H., et al. (2010). Significant portion of dissolved organic Fe complexes in fact is Fe colloids. *Marine Chemistry*, *122*(1–4), 20–27. https://doi.org/10.1016/j.marchem.2010.09.001

Browning, T. J., Achterberg, E. P., Engel, A., & Mawji, E. (2021). Manganese co-limitation of phytoplankton growth and major nutrient drawdown in the Southern Ocean. *Nature Communications*, *12*(1), 884. https://doi.org/10.1038/s41467-021-21122-6

Browning, T. J., & Moore, C. M. (2023). Global analysis of ocean phytoplankton nutrient limitation reveals high prevalence of co-limitation. *Nature Communications*, *14*(1), 5014. https://doi.org/10.1038/s41467-023-40774-0

Buesseler, K. O., Benitez-Nelson, C. R., Roca-Martí, M., Wyatt, A. M., Resplandy, L., Clevenger, S. J., et al. (2020). High-resolution spatial and temporal measurements of particulate organic carbon flux using thorium-234 in the northeast Pacific Ocean during the EXport Processes in the Ocean from RemoTe sensing field campaign. *Elementa: Science of the Anthropocene*, *8*(1), 030. https://doi.org/10.1525/elementa.2020.030

Cabanes, D. J. E., Norman, L., Santos-Echeandía, J., Iversen, M. H., Trimborn, S., Laglera, L. M., & Hassler, C. S. (2017). First evaluation of the role of salp fecal pellets on iron biogeochemistry. *Frontiers in Marine Science*, *3*. https://doi.org/10.3389/fmars.2016.00289

Canário, J., Santos-Echeandia, J., Padeiro, A., Amaro, E., Strass, V., Klaas, C., et al. (2017). Mercury and methylmercury in the Atlantic sector of the Southern Ocean. *Deep Sea Research Part II: Topical Studies in Oceanography*, *138*, 52–62. https://doi.org/10.1016/j.dsr2.2016.07.012

Caron, D. A., Madin, L. P., & Cole, J. J. (1989). Composition and degradation of salp fecal pellets: Implications for vertical flux in oceanic environments. *Journal of Marine Research*, *47*(4), 829–850. https://doi.org/10.1357/002224089785076118

Chance, R., Jickells, T. D., & Baker, A. R. (2015). Atmospheric trace metal concentrations, solubility and deposition fluxes in remote marine air over the south-east Atlantic. *Marine Chemistry*, *177*(Part 1), 45–56. https://doi.org/10.1016/j.marchem.2015.06.028

Cheah, W., Soppa, M. A., Wiegmann, S., Ossebaar, S., Laglera, L. M., Strass, V. H., et al. (2017). Importance of deep mixing and silicic acid in regulating phytoplankton biomass and community in the iron-limited Antarctic Polar Front region in summer. *Deep-Sea Research Part II Topical Studies in Oceanography*, *138*, 74–85. https://doi.org/10.1016/j.dsr2.2016.05.019

Chen, M., Wang, W.-X., & Guo, L. (2004). Phase partitioning and solubility of iron in natural seawater controlled by dissolved organic matter. *Global Biogeochemical Cycles*, *18*(4). https://doi.org/10.1029/2003GB002160

Croot, P. L., Frew, R. D., Sander, S., Hunter, K. A., Ellwood, M. J., Pickmere, S. E., et al. (2007). Physical mixing effects on iron biogeochemical cycling: FeCycle experiment. *Journal of Geophysical Research: Oceans*, *112*(6). https://doi.org/10.1029/2006jc003748

Croot, P. L., & Laan, P. (2002). Continuous shipboard determination of Fe(II) in polar waters using flow injection analysis with chemiluminescence detection. *Analytica Chimica Acta*, *466*(2), 261–273. https://doi.org/10.1016/S0003-2670(02)00596-2

Cutter, G., Casciotti, K., Croot, P., Geibert, W., Heimbürger, L.-E., Lohan, M., et al. (2017). Sampling and sample-handling protocols for GEOTRACES cruises. Version 3, August 2017.

de Baar, H. J. W., de Jong, J. T. M., Bakker, D. C. E., Loscher, B. M., Veth, C., Bathmann, U., & Smetacek, V. (1995). Importance of iron for plankton blooms and carbon dioxide drawdown in the Southern Ocean. *Nature*, *373*(6513), 412–415. https://doi.org/10.1038/373412a0

de Jong, J., Schoemann, V., Lannuzel, D., Croot, P., De Baar, H., & Tison, J. L. (2012). Natural iron fertilization of the Atlantic sector of the Southern Ocean by continental shelf sources of the Antarctic Peninsula. *Journal of Geophysical Research: Biogeosciences*, *117*(1). https://doi.org/10.1029/2011JG001679

de Jong, J., Schoemann, V., Maricq, N., Mattielli, N., Langhorne, P., Haskell, T., & Tison, J.-L. (2013). Iron in land-fast sea ice of McMurdo Sound derived from sediment resuspension and wind-blown dust attributes to primary productivity in the Ross Sea, Antarctica. *Marine Chemistry*, *157*, 24–40. https://doi.org/10.1016/j.marchem.2013.07.001

Fitzsimmons, J. N., Carrasco, G. G., Wu, J., Roshan, S., Hatta, M., Measures, C. I., et al. (2015). Partitioning of dissolved iron and iron isotopes into soluble and colloidal phases along the GA03 GEOTRACES North Atlantic Transect. *Deep Sea Research Part II: Topical Studies in Oceanography*, *116*, 130–151. https://doi.org/10.1016/j.dsr2.2014.11.014

Flynn, K. J., Atkinson, A., Beardall, J., Berges, J. A., Boersma, M., Brunet, C., et al. (2025). More realistic plankton simulation models will improve projections of ocean ecosystem responses to global change. *Nature Ecology & Evolution*, 1–9. https://doi.org/10.1126/sciadv.adi3059

Frew, R. D., Hutchins, D. A., Nodder, S., Sanudo-Wilhelmy, S., Tovar-Sanchez, A., Leblanc, K., et al. (2006). Particulate iron dynamics during FeCycle in subantarctic waters southeast of New Zealand. *Global Biogeochemical Cycles*, *20*(1). https://doi.org/10.1029/2005GB002558

Gledhill, M., & Buck, K. N. (2012). The organic complexation of iron in the marine environment: A review. *Frontiers in Microbiology*, *3*, 1–19. https://doi.org/10.3389/fmicb.2012.00069

Henson, S. A., Briggs, N., Carvalho, F., Manno, C., Mignot, A., & Thomalla, S. (2023). A seasonal transition in biological carbon pump efficiency in the northern Scotia Sea, Southern Ocean. *Deep Sea Research Part II: Topical Studies in Oceanography*, *208*, 105274. https://doi.org/10.1016/j.dsr2.2023.105274

Hopkinson, B. M., Seegers, B., Hatta, M., Measures, C. I., Greg Mitchell, B., & Barbeau, K. A. (2013). Planktonic C: Fe ratios and carrying capacity in the southern Drake Passage. *Deep-Sea Research Part II Topical Studies in Oceanography*, *90*, 102–111. https://doi.org/10.1016/j.dsr2.2012.09.001

Hoppe, C. J. M., Klaas, C., Ossebaar, S., Soppa, M., Cheah, W., Laglera, L., et al. (2017). Controls of primary production in two phytoplankton blooms in the Antarctic Circumpolar Current. *Deep Sea Research Part II: Topical Studies in Oceanography*, *138*, 63–73. https://doi.org/10.1016/j.dsr2.2015.10.005

Ito, A., & Shi, Z. (2016). Delivery of anthropogenic bioavailable iron from mineral dust and combustion aerosols to the ocean. *Atmospheric Chemistry and Physics*, *16*(1), 85–99. https://doi.org/10.5194/acp-16-85-2016

Iversen, M. H., Pakhomov, E. A., Hunt, B. P., van der Jagt, H., Wolf-Gladrow, D., & Klaas, C. (2017). Sinkers or floaters? Contribution from salp pellets to the export flux during a large bloom event in the Southern Ocean. *Deep Sea Research Part II: Topical Studies in Oceanography*, *138*, 116–125. https://doi.org/10.1016/j.dsr2.2016.12.004

Iversen, M. H., & Poulsen, L. K. (2007). Coprorhexy, coprophagy, and coprochaly in the copepods Calanus helgolandicus, Pseudocalanus elongatus, and Oithona similis. *Marine Ecology Progress Series*, *350*, 79–89. https://doi.org/10.3354/meps07095

Johnson, K. S., Elrod, V., Fitzwater, S., Plant, J., Boyle, E., Bergquist, B., et al. (2007). Developing standards for dissolved iron in seawater. *Eos*, *88*(11), 131–132. https://doi.org/10.1029/2007EO110003

Johnson, K. S., Michael Gordon, R., & Coale, K. H. (1997). What controls dissolved iron concentrations in the world ocean? *Marine Chemistry*, *57*(3–4), 137–161. https://doi.org/10.1016/S0304-4203(97)00043-1

Klunder, M. B., Laan, P., Middag, R., De Baar, H. J. W., & van Ooijen, J. C. (2011). Dissolved iron in the Southern Ocean (Atlantic sector). *Deep Sea Research Part II: Topical Studies in Oceanography*, *58*(25–26), 2678–2694. https://doi.org/10.1016/j.dsr2.2010.10.042

Kondo, Y., Takeda, S., Nishioka, J., Obata, H., Furuya, K., Johnson, W. K., & Wong, C. S. (2008). Organic iron (III) complexing ligands during an iron enrichment experiment in the western subarctic North Pacific. *Geophysical Research Letters*, *35*(12). https://doi.org/10.1029/2008GL033354

Laglera, L. M., Santos-Echeandia, J., Caprara, S., & Monticelli, D. (2013). Quantification of iron in seawater at the low picomolar range based on optimization of bromate/ammonia/dihydroxynaphtalene system by catalytic adsorptive cathodic stripping voltammetry. *Analytical Chemistry*, *85*(4), 2486–2492. https://doi.org/10.1021/ac303621q

Laglera, L. M., Santos-Echeandía, J., Fischer, L., & Hann, S. (2025a). Iron partitioning in the upper 300 m of the water column during the cruise ANT-XXVIII/3 in waters of the Southern Ocean [Dataset]. *PANGAEA*. https://doi.org/10.1594/PANGAEA.951782

Laglera, L. M., Santos-Echeandía, J., Fischer, L., & Hann, S. (2025b). Iron partitioning at a single station north of South Georgia during POLARSTERN cruise ANT-XXVIII/3 [Dataset]. *PANGAEA*. https://doi.org/10.1594/PANGAEA.951902

Laglera, L. M., Tovar-Sánchez, A., Iversen, M., González, H., Naik, H., Mangesh, G., et al. (2017). Iron partitioning during LOHAFEX: Copepod grazing as a major driver for iron recycling in the Southern Ocean. *Marine Chemistry*, *196*, 148–161. https://doi.org/10.1016/j.marchem.2017.08.011

Laglera, L. M., Tovar-Sanchez, A., Sukekava, C. F., Naik, H., Naqvi, S. W. A., & Wolf-Gladrow, D. A. (2020). Iron organic speciation during the LOHAFEX experiment: Iron ligands release under biomass control by copepod grazing. *Journal of Marine Systems*, *207*, 103151. https://doi.org/10.1016/j.jmarsys.2019.02.002

Laglera, L. M., Uskaikar, H., Klaas, C., Naqvi, S. W. A., Wolf-Gladrow, D. A., & Tovar-Sánchez, A. (2022). Dissolved and particulate iron redox speciation during the LOHAFEX fertilization experiment. *Marine Pollution Bulletin*, *184*, 114161. https://doi.org/10.1016/j.marpolbul.2022.114161

Lannuzel, D., Van der Merwe, P. C., Townsend, A. T., & Bowie, A. R. (2014). Size fractionation of iron, manganese and aluminium in Antarctic fast ice reveals a lithogenic origin and low iron solubility. *Marine Chemistry*, *161*, 47–56. https://doi.org/10.1016/j.marchem.2014.02.006

Lemaitre, N., Planquette, H., Dehairs, F., Planchon, F., Sarthou, G., Gallinari, M., et al. (2020). Particulate trace element export in the North Atlantic (GEOTRACES GA01 transect, GEOVIDE cruise). *ACS Earth and Space Chemistry*, *4*(11), 2185–2204. https://doi.org/10.1021/acsearthspacechem.0c00045

Le Mézo, P. K., & Galbraith, E. D. (2021). The fecal iron pump: Global impact of animals on the iron stoichiometry of marine sinking particles. *Limnology & Oceanography*, *66*(1), 201–213. https://doi.org/10.1002/lno.11597

Li, J., Babcock-Adams, L., Boiteau, R. M., McIlvin, M. R., Manck, L. E., Sieber, M., et al. (2024). Microbial iron limitation in the ocean's twilight zone. *Nature*, *633*(8031), 823–827. https://doi.org/10.1038/s41586-024-07905-z

Maranger, R., Bird, D. F., & Price, N. M. (1998). Iron acquisition by photosynthetic marine phytoplankton from ingested bacteria. *Nature*, *396*(6708), 248–251. https://doi.org/10.1038/24352

Martiny, A. C., Pham, C. T. A., Primeau, F. W., Vrugt, J. A., Moore, J. K., Levin, S. A., & Lomas, M. W. (2013). Strong latitudinal patterns in the elemental ratios of marine plankton and organic matter. *Nature Geoscience*, *6*(4), 279–283. https://doi.org/10.1038/ngeo1757

Mazzocchi, M. G., González, H. E., Vandromme, P., Borrione, I., Ribera d'Alcalà, M., Gauns, M., et al. (2009). A non-diatom plankton bloom controlled by copepod grazing and amphipod predation: Preliminary results from the LOHAFEX iron-fertilisation experiment. *GLOBEC International Newsletter* (15), 3–6.

Mendez, J., Guieu, C., & Adkins, J. (2010). Atmospheric input of manganese and iron to the ocean: Seawater dissolution experiments with Saharan and North American dusts. *Marine Chemistry*, *120*(1), 34–43. https://doi.org/10.1016/j.marchem.2008.08.006

Meredith, M. P., Watkins, J. L., Murphy, E. J., Ward, P., Bone, D. G., Thorpe, S. E., et al. (2003). Southern ACC Front to the northeast of South Georgia: Pathways, characteristics, and fluxes. *Journal of Geophysical Research*, *108*(C5). https://doi.org/10.1029/2001JC001227

Misumi, K., Nishioka, J., Obata, H., Tsumune, D., Tsubono, T., Long, M. C., et al. (2021). Slowly sinking particles underlie dissolved iron transport across the Pacific Ocean. *Global Biogeochemical Cycles*, *35*(4), e2020GB006823. https://doi.org/10.1029/2020GB006823

Morrison, A. K., Frölicher, T. L., & Sarmiento, J. L. (2015). Upwelling in the southern ocean. *Physics Today*, *68*(1), 27–32. https://doi.org/10.1063/PT.3.2654

Nielsdóttir, M. C., Bibby, T. S., Moore, C. M., Hinz, D. J., Sanders, R., Whitehouse, M., et al. (2012). Seasonal and spatial dynamics of iron availability in the Scotia Sea. *Marine Chemistry*, *130–131*, 62–72. https://doi.org/10.1016/j.marchem.2011.12.004

Nishioka, J., Takeda, S., de Baar, H. J. W., Croot, P. L., Boye, M., Laan, P., & Timmermans, K. R. (2005). Changes in the concentration of iron in different size fractions during an iron enrichment experiment in the open Southern Ocean. *Marine Chemistry*, *95*(1–2), 51–63. https://doi.org/10.1016/j.marchem.2004.06.040

Obernosterer, I., Fourquez, M., & Blain, S. (2015). Fe and C co-limitation of heterotrophic bacteria in the naturally fertilized region off the Kerguelen Islands. *Biogeosciences*, *12*(6), 1983–1992. https://doi.org/10.5194/bg-12-1983-2015

Pakhomov, E. A., & Hunt, B. P. (2017). Trans-Atlantic variability in ecology of the pelagic tunicate Salpa thompsoni near the Antarctic Polar Front. *Deep Sea Research Part II: Topical Studies in Oceanography*, *138*, 126–140. https://doi.org/10.1016/j.dsr2.2017.03.001

Planquette, H., Fones, G. R., Statham, P. J., & Morris, P. J. (2009). Origin of iron and aluminium in large particles (>53 μm) in the Crozet region, Southern Ocean. *Marine Chemistry*, *115*(1), 31–42. https://doi.org/10.1016/j.marchem.2009.06.002

Planquette, H., Sherrell, R. M., Stammerjohn, S., & Field, M. P. (2013). Particulate iron delivery to the water column of the Amundsen Sea, Antarctica. *Marine Chemistry*, *153*, 15–30. https://doi.org/10.1016/j.marchem.2013.04.006

Planquette, H., Statham, P. J., Fones, G. R., Charette, M. A., Moore, C. M., Salter, I., et al. (2007). Dissolved iron in the vicinity of the Crozet Islands, Southern Ocean. *Deep Sea Research Part II: Topical Studies in Oceanography*, *54*(18–20), 1999–2019. https://doi.org/10.1016/j.dsr2.2007.06.019

Pollard, R. T., Bathmann, U., Dubischar, C., Read, J. F., & Lucas, M. (2002). Zooplankton distribution and behaviour in the Southern Ocean from surveys with a towed Optical Plankton Counter. *Deep-Sea Research Part II Topical Studies in Oceanography*, *49*(18), 3889–3915. https://doi.org/10.1016/S0967-0645(02)00116-9

Poulsen, L. K., & Iversen, M. H. (2008). Degradation of copepod fecal pellets: Key role of protozooplankton. *Marine Ecology Progress Series*, *367*, 1–13. https://doi.org/10.3354/meps07611

Puigcorbé, V., Roca-Martí, M., Masqué, P., Benitez-Nelson, C. R., Rutgers v. d. Loeff, M., Laglera, L. M., et al. (2017). Particulate organic carbon export across the Antarctic Circumpolar Current at 10°E: Differences between north and south of the Antarctic Polar Front. *Deep Sea Research Part II: Topical Studies in Oceanography*, *138*, 86–101. https://doi.org/10.1016/j.dsr2.2016.05.016

Raiswell, R. (2011). Iceberg-hosted nanoparticulate Fe in the Southern Ocean: Mineralogy, origin, dissolution kinetics and source of bioavailable Fe. *Deep-Sea Research Part II Topical Studies in Oceanography*, *58*(11–12), 1364–1375. https://doi.org/10.1016/j.dsr2.2010.11.011

Ratnarajah, L., & Bowie, A. R. (2016). Nutrient cycling: Are Antarctic krill a previously overlooked source in the marine iron cycle? *Current Biology*, *26*(19), R884–R887. https://doi.org/10.1016/j.cub.2016.08.044

Revels, B. N., Ohnemus, D. C., Lam, P. J., Conway, T. M., & John, S. G. (2015). The isotopic signature and distribution of particulate iron in the North Atlantic Ocean. *Deep Sea Research Part II: Topical Studies in Oceanography*, *116*, 321–331. https://doi.org/10.1016/j.dsr2.2014.12.004

Roca-Martí, M., Puigcorbé, V., Iversen, M. H., van der Loeff, M. R., Klaas, C., Cheah, W., et al. (2017). High particulate organic carbon export during the decline of a vast diatom bloom in the Atlantic sector of the Southern Ocean. *Deep Sea Research Part II: Topical Studies in Oceanography*, *138*, 102–115. https://doi.org/10.1016/j.dsr2.2015.12.007

Sabine, C. L., Feely, R. A., Gruber, N., Key, R. M., Lee, K., Bullister, J. L., et al. (2004). The oceanic sink for anthropogenic CO_2. *Science*, *305*(5682), 367–371. https://doi.org/10.1126/science.1097403

Sato, M., Takeda, S., & Furuya, K. (2009). Responses of pico- and nanophytoplankton to artificial iron infusions observed during the second iron enrichment experiment in the western subarctic Pacific (SEEDS II). *Deep Sea Research Part II: Topical Studies in Oceanography*, *56*(26), 2745–2754. https://doi.org/10.1016/j.dsr2.2009.06.002

Schlitzer, R., Anderson, R. F., Dodas, E. M., Lohan, M., Geibert, W., Tagliabue, A., et al. (2018). The GEOTRACES Intermediate Data Product 2017. *Chemical Geology*, *493*, 210–223. https://doi.org/10.1016/j.chemgeo.2018.05.040

Schlosser, C., Schmidt, K., Aquilina, A., Homoky, W. B., Castrillejo, M., Mills, R. A., et al. (2018). Mechanisms of dissolved and labile particulate iron supply to shelf waters and phytoplankton blooms off South Georgia, Southern Ocean. *Biogeosciences*, *15*(16), 4973–4993. https://doi.org/10.5194/bg-15-4973-2018

Seo, H., Kim, G., Kim, T., Kim, I., Ra, K., & Jeong, H. (2022). Trace elements (fe, Mn, Co, Cu, Cd, and Ni) in the East Sea (Japan Sea): Distributions, boundary inputs, and scavenging processes. *Marine Chemistry*, *239*, 104070. https://doi.org/10.1016/j.marchem.2021.104070

Shaked, Y., Buck, K. N., Mellett, T., & Maldonado, M. T. (2020). Insights into the bioavailability of oceanic dissolved Fe from phytoplankton uptake kinetics. *ISME Journal*, *14*(5), 1182–1193. https://doi.org/10.1038/s41396-020-0597-3

Shaked, Y., & Lis, H. (2012). Disassembling iron availability to phytoplankton. *Frontiers in Microbiology*, *3*. https://doi.org/10.3389/fmicb.2012.00123

Shi, Z., Bonneville, S., Krom, M. D., Carslaw, K. S., Jickells, T. D., Baker, A. R., & Benning, L. G. (2011). Iron dissolution kinetics of mineral dust at low pH during simulated atmospheric processing. *Atmospheric Chemistry and Physics*, *11*(3), 995–1007. https://doi.org/10.5194/acp-11-995-2011

Sieber, M., Conway, T. M., de Souza, G. F., Hassler, C. S., Ellwood, M. J., & Vance, D. (2021). Isotopic fingerprinting of biogeochemical processes and iron sources in the iron-limited surface Southern Ocean. *Earth and Planetary Science Letters*, *567*, 116967. https://doi.org/10.1016/j.epsl.2021.116967

Smetacek, V., Assmy, P., & Henjes, J. (2004). The role of grazing in structuring Southern Ocean pelagic ecosystems and biogeochemical cycles. *Antarctic Science*, *16*(4), 541–558. https://doi.org/10.1017/S0954102004002317

Smetacek, V., Klaas, C., Strass, V. H., Assmy, P., Montresor, M., Cisewski, B., et al. (2012). Deep carbon export from a Southern Ocean iron-fertilized diatom bloom. *Nature*, *487*(7407), 313–319. https://doi.org/10.1038/nature11229

Strass, V. H., Leach, H., Prandke, H., Donnelly, M., Bracher, A. U., & Wolf-Gladrow, D. A. (2017). The physical environmental conditions for biogeochemical differences along the Antarctic Circumpolar Current in the Atlantic Sector during late austral summer 2012. *Deep-Sea Research Part II Topical Studies in Oceanography*, *138*, 6–25. https://doi.org/10.1016/j.dsr2.2016.05.018

Strass, V. H., Wolf-Gladrow, D., Pakhomov, E. A., & Klaas, C. (2017). Eddy-Pump: Pelagic carbon pump processes along the eddying Antarctic Polar Front in the Atlantic Sector of the Southern Ocean. *Deep-Sea Research Part II Topical Studies in Oceanography*, *138*, 1–5. https://doi.org/10.1016/j.dsr2.2017.02.009

Sunda, W. G., & Huntsman, S. A. (1995). Iron uptake and growth limitation in oceanic and coastal phytoplankton. *Marine Chemistry*, *50*(1–4), 189–206. https://doi.org/10.1016/0304-4203(95)00035-P

Tagliabue, A., Bowie, A. R., Boyd, P. W., Buck, K. N., Johnson, K. S., & Saito, M. A. (2017). The integral role of iron in ocean biogeochemistry. *Nature*, *543*(7643), 51–59. https://doi.org/10.1038/nature21058

Tagliabue, A., Buck, K. N., Sofen, L. E., Twining, B. S., Aumont, O., Boyd, P. W., et al. (2023). Authigenic mineral phases as a driver of the upper-ocean iron cycle. *Nature*, *620*(7972), 104–109. https://doi.org/10.1038/s41586-023-06210-5

Trimborn, S., Brenneis, T., Hoppe, C. J. M., Laglera, L. M., Norman, L., Santos-Echeandía, J., et al. (2017). Iron sources alter the response of Southern Ocean phytoplankton to ocean acidification. *Marine Ecology Progress Series*, *578*, 35–50. https://doi.org/10.3354/meps12250

Twining, B. S. (2024). An ocean of particles characterization of particulate trace elements by the GEOTRACES program. *Oceanography*, *37*(2). https://doi.org/10.5670/oceanog.2024.407

Twining, B. S., & Baines, S. B. (2013). The trace metal composition of marine phytoplankton. *Annual Review of Marine Science*, *5*(1), 191–215. https://doi.org/10.1146/annurev-marine-121211-172322

von der Heyden, B. P., & Roychoudhury, A. N. (2015). A review of colloidal iron partitioning and distribution in the open ocean. *Marine Chemistry*, *177*(Part 1), 9–19. https://doi.org/10.1016/j.marchem.2015.05.010

Wen, L. S., Stordal, M. C., Tang, D. G., Gill, G. A., & Santschi, P. H. (1996). An ultraclean cross-flow ultrafiltration technique for the study of trace-metal phase speciation in seawater. *Marine Chemistry*, *55*(1–2), 129–152. https://doi.org/10.1016/S0304-4203(96)00052-7

Wolf-Gladrow, D. (2013). *The expedition of the research vessel "Polarstern" to the Antarctic in 2012 (ANT-XXVIII/3)Report* (p. 191). Alfred-Wegener-Institut Helmholtz-Zentrum für Polar und Meeresforschung.